UNIVERSITÉ DU QUÉBEC À TROIS–RIVIÈRES

COMPUTATIONAL OPTIMIZATION OF MULTILAYER ANODE ARCHITECTURES FOR HIGH–ENERGY LITHIUM–ION BATTERIES

DISSERTATION PRESENTED
AS PARTIAL REQUIREMENT FOR THE
MASTER'S DEGREE IN MECHANICAL ENGINEERING

BY
JUAN CAMILO RUBIO RODRIGUEZ

JUILLET 2025

UNIVERSITÉ DU QUÉBEC À TROIS–RIVIÈRES
MAÎTRISE EN GÉNIE MÉCANIQUE

Direction de recherche:

Martin Bolduc
Prénom Nom — Directeur de recherche

Jury d'évaluation

Alben Cardenas, Universidad de Quebec en Trois-Rivières (UQTR)
Prénom Nom, Nom établissement — Évaluateur interne

Sylvain Cloutier, École de technologie supérieure (ETS)
Prénom Nom, Nom établissement — Évaluateur externe

Martin Bolduc, Universidad de Quebec en Trois-Rivières (UQTR)
Prénom Nom, Nom établissement — Directeur de recherche

ACKNOWLEDGMENTS

This work would not have been possible without the support of several important individuals in my life, to whom I wish to express my sincere gratitude.

To my parents, Flor Alba Rodríguez Santos and José Vicente Rubio Giraldo, for their tireless dedication, essential role as parents, and constant presence throughout my academic journey.

To my wife, for her patience, unwavering support, and the stability she has brought to our home, allowing me to fully dedicate myself to research.

I also extend my deep gratitude to my supervisor, Martin Bolduc, for his trust, constant guidance, and invaluable advice throughout this process.

Finally, I thank the Université du Québec à Trois–Rivières (UQTR) for its administrative and educational support, as well as the quality of its training.

ABSTRACT

This thesis addresses the computational optimization of multilayer anode architectures aimed at enhancing the performance of high–energy lithium–ion batteries. Given the critical need for improved energy density, cycle life, and sustainability, this research evaluates multilayer anode designs that strategically combine graphite with silicon and other alternative materials (hard carbon, lithium titanate oxide (LTO), and lithium metal). It validates a simulation–driven workflow for designing multilayer lithium–ion–battery anodes that raise specific energy without sacrificing long–term stability. Finite–element electrochemical modelling in COMSOL Multiphysics®, coupled with factorial and multivariate statistics in JMP®, is used to isolate the geometric and compositional variables that govern capacity fade, solid–electrolyte–interphase (SEI) growth, overpotential and electrolyte loss.

In Phase I a 3^3 full factorial varies silicon content (10–30 wt %), graphite particle size (2.5–7.5 μm) and layer–thickness ratio (10–50, 20–40, 30–30 μm) across twenty–seven graphite / graphite–silicon bilayers cycled 2 000 times at 1 C. The optimal configuration consists of a 30 μm graphite buffer layer over a 30 μm composite containing approximately 20 wt% silicon and 2.5 μm graphite particles. This setup limits capacity fade to around 20%, caps SEI thickness at 0.36 μm, maintains the SEI overpotential at 42 mV, and consumes only 44% of the initial electrolyte. It outperforms both a 100% graphite electrode and a homogeneous 90% graphite / 10% silicon blend by reducing direct electrolyte contact with silicon and promoting a more uniform current distribution.

Phase II takes that graphite buffer and particle size while replacing the inner composite with hard carbon, $Li_4Ti_5O_{12}$ (LTO) or metallic lithium, each tested pure and as 10/20/30 wt % graphite mixtures. Among sixteen new cells, one stands out because it has a second layer with 100% hard–carbon core that retains ≈94 % of its initial capacity with negligible impedance rise. Another with a second layer of 10 wt % LTO generates the

thinnest SEI (0.17 μm) and the lowest electrolyte loss (~19 %) while sacrificing only 11.5 % capacity, and finally, a configuration with a second layer with 30 wt % Li–metal delivers the largest gravimetric capacity gain but stabilizes at ~83 % retention because of dead–lithium formation and higher mid–SOC polarization.

Electrochemical impedance spectroscopy confirms that the graphite buffer effectively decouples SEI resistance from charge–transfer resistance, while the inner layer material dictates diffusional impedance and kinetic durability. This study provides a practical design framework: employ balanced layer thicknesses to facilitate diffusion processes and avoid bottlenecks. A graphite front layer with fine particles is recommended to control SEI chemistry, paired with a second high–capacity layer tailored to specific applications silicon–rich or lithium metal for high energy density, hard carbon for rapid charge resilience, or LTO for safety–critical, long–life battery packs thereby offering a scalable route to pouch cells suitable for electric vehicles and grid storage.

Keywords: Multilayer anode; graphite buffer; silicon composite; hard carbon; lithium titanate oxide; lithium metal; COMSOL simulation; factorial design; SEI mitigation; capacity retention.

RÉSUMÉ

Ce mémoire porte sur l'optimisation computationnelle d'architectures d'anodes multicouches visant à améliorer les performances des batteries lithium–ion à haute densité énergétique. Compte tenu du besoin critique d'améliorer la densité énergétique, la durée de vie des cycles et la durabilité, cette recherche évalue des conceptions d'anodes multicouches combinant stratégiquement le graphite avec du silicium et d'autres matériaux alternatifs (carbone dur, oxyde de lithium–titane (LTO) et lithium métallique). Elle valide une démarche basée sur la simulation pour la conception d'anodes multicouches de batteries lithium–ion, augmentant l'énergie spécifique sans compromettre la stabilité à long terme. La modélisation électrochimique par éléments finis dans COMSOL Multiphysics®, couplée à des analyses statistiques factorielles et multivariées réalisées avec JMP®, permet d'isoler les variables géométriques et compositionnelles contrôlant la perte de capacité, la croissance de l'interface solide–électrolyte (SEI), la surtension et la perte d'électrolyte.

Dans la phase I, un plan factoriel complet 3^3 fait varier la teneur en silicium (10–30 % en masse), la taille des particules de graphite (2,5–7,5 µm) et le rapport d'épaisseur des couches (10–50, 20–40, 30–30 µm) sur vingt–sept configurations bicouches graphite / graphite–silicium, cyclées 2 000 fois à 1 C. La configuration optimale identifiée consiste en une couche tampon de graphite de 30 µm sur une couche composite de 30 µm contenant environ 20 % en masse de silicium et des particules de graphite de 2,5 µm, limitant ainsi la perte de capacité à environ 20 %, l'épaisseur de la SEI à 0,36 µm, maintenant la surtension de la SEI à 42 mV et consommant seulement 44 % de l'électrolyte initial. Cette configuration surpasse à la fois une couche 100 % graphite et une configuration homogène à 90 % graphite / 10 % silicium, en évitant le contact direct entre l'électrolyte et le silicium et en uniformisant la distribution du courant.

Dans la phase II, ce tampon de graphite optimisé et la taille des particules sont maintenus, tandis que le composite interne est remplacé par du carbone dur, du $Li_4Ti_5O_{12}$ (LTO) ou du lithium métallique, chacun testé pur ou mélangé à 10, 20 ou 30 % en masse de graphite. Parmi seize nouvelles configurations de cellules évaluées, une se démarque avec une seconde couche entièrement composée de carbone dur, conservant environ 94 % de sa capacité initiale avec une hausse d'impédance négligeable. Une autre, avec 10 % en masse de LTO dans la deuxième couche, génère la SEI la plus fine (0,17 µm) et la perte d'électrolyte la plus faible (~19 %), tout en ne sacrifiant que 11,5 % de capacité. Enfin, une configuration avec une deuxième couche contenant 30 % en masse de lithium métallique atteint le gain de capacité gravimétrique le plus élevé, mais stabilise autour de 83 % de rétention à cause de la formation de lithium mort et d'une polarisation accrue à mi–état de charge (SOC).

La spectroscopie d'impédance électrochimique confirme que le tampon de graphite découple efficacement la résistance SEI de la résistance au transfert de charge, tandis que le matériau interne dicte l'impédance de diffusion et la durabilité cinétique. Cette étude fournit un cadre de conception pratique : employer des couches équilibrées en épaisseur pour faciliter les processus de diffusion et éviter les goulots d'étranglement. Une couche frontale de graphite avec des particules fines est recommandée pour contrôler la chimie de la SEI, associée à une seconde couche à haute capacité adaptée aux applications spécifiques : riche en silicium ou lithium métallique pour une haute densité énergétique, carbone dur pour une résilience en charge rapide, ou LTO pour des packs de batteries de longue durée et de sécurité critique, offrant ainsi une voie évolutive vers des cellules en poche adaptées aux véhicules électriques et au stockage en réseau.

Mots–clés: Anode multicouche ; tampon de graphite ; composite silicium ; carbone dur ; oxyde de lithium–titane ; lithium métallique ; simulation COMSOL ; plan factoriel ; atténuation SEI ; rétention de capacité.

TABLE OF CONTENTS

LIST OF TABLES

LIST OF FIGURES

LIST OF ABBREVIATIONS

JMP	JMP Statistical Discovery Software
SEI	Solid Electrolyte Interphase
SOC	State of Charge
LTO	Lithium Titanate Oxide
NMC622	$LiNi_{0.6}Mn_{0.2}Co_{0.2}O_2$ cathode
EC	Ethylene Carbonate
EMC	Ethyl Methyl Carbonate
$LiPF_6$	Lithium Hexafluorophosphate
CNT	Carbon Nanotube
MWCNT	Multi–Walled Carbon Nanotube
CNF	Carbon Nanofiber
rGO	Reduced Graphene Oxide
SWCNT	Single–Walled Carbon Nanotube
TWh	Terawatt–hour
Wh/kg	Watt–hour per kilogram
mAh/g	Milliampere–hour per gram
ANOVA	Analysis of Variance
MANOVA	Multivariate Analysis of Variance
R_{ct}	Charge–Transfer Resistance
R_{SEI}	SEI Resistance
Rs	Series/Electrolyte Resistance
1C	Charge rate of 1 C
1D	One–Dimensional
3D	Three–Dimensional
LCO	Lithium Cobalt Oxide
ML	Lithium Metal

LIST OF SYMBOLS

κ_{eff}	Effective ionic conductivity of the electrolyte ($S \cdot m^{-1}$)
κ	Intrinsic ionic conductivity of the electrolyte ($S \cdot m^{-1}$)
ε	Electrode porosity
brugg	Bruggeman exponent (tortuosity factor)
c_s	Lithium concentration in the solid phase ($mol \cdot m^{-3}$)
t	Time (s)
r	Radial coordinate within particle (m)
D_{eff}	Effective diffusion coefficient in the solid ($m^2 \cdot s^{-1}$)
i_{loc}	Local current density ($A \cdot m^{-2}$)
i_0	Exchange current density ($A \cdot m^{-2}$)
η	Reaction overpotential (V)
α_a, αc	Anodic and cathodic charge transfer coefficients
a	Specific surface area of the electrode ($m^2 \cdot m^{-3}$)
σ_s	Electronic conductivity of the solid ($S \cdot m^{-1}$)
ϕ_s	Electric potential in the solid (V)
ϕ_l	Electric potential in the electrolyte (V)
t^+	Lithium–ion transference number in the electrolyte
c_l	Lithium–ion concentration in the electrolyte ($mol \cdot m^{-3}$)
R	Gas constant ($8.314\ J \cdot mol^{-1} \cdot K^{-1}$)
T	Absolute temperature (K)
F	Faraday constant ($96{,}485\ C \cdot mol^{-1}$)
SOC	State of Charge = c_s / c_{max}
H_k	Graphite expansion factor (function of SOC)
J	Parasitic exchange current density
q_{SEI}	Charge accumulated in the SEI layer ($C \cdot m^{-2}$)
f	Lumped kinetic parameter of SEI growth (s^{-1})
$i_{0,ref}$	Local current at 1C reference
δ_{film}	SEI film thickness (m)

κ_{film}	SEI layer conductivity (S·m⁻¹)
R_{film}	Resistance of the SEI layer (Ω·m²)
M_{SEI}	Molar mass
A_{f}	Effective surface area for SEI growth (m²)
ρ_{SEI}	Density of the SEI layer (kg·m⁻³)
$\delta_{\text{film,0}}$	Initial SEI thickness (m)
ν_{SEI}	Stoichiometric coefficient of SEI–formation reaction
n	Number of electrons transferred per reaction
τ	Time–acceleration (aging) factor (dimensionless)
i_{s}	Electronic current density in the solid (A·m⁻²)
i_{l}	Ionic current density in the electrolyte (A·m⁻²)
f_{G}	Volume fraction of graphite–only phase in anode
$f_{\text{G+S}}$	Volume fraction of graphite+Si phase
i_{G}	Local current density in graphite phase (A·m⁻²)
$i_{\text{G+S}}$	Local current density in graphite+Si phase (A·m⁻²)
c_{SEI}	SEI–phase concentration (mol·m⁻³)
R_{s}	Series (ohmic) resistance (Ω)
R_{ct}	Charge–transfer resistance (Ω)
Z'	Real part of complex impedance (Ω)
Z''	Imaginary part of complex impedance (Ω)
$\|Z\|$	Impedance modulus (Ω)
σ_{W}	Warburg coefficient (Ω·s$^{-1/2}$)
C_{dl}	Double–layer capacitance (F)
C_{SEI}	SEI–layer capacitance (F)
ω	Angular frequency, ω = 2πf (rad·s⁻¹)
$c_{s,\text{max}}$	Maximum Li–ion concentration inside a single active–material particle (mol · m⁻³)
c_{max}	Maximum Li inventory per unit volume of porous electrode (mol · m⁻³)
Γ_{Cu}	Boundary surface in contact with the negative (copper) current collector.
Γ_{Al}	Boundary surface in contact with the positive (Aluminium) current collector.
I_{app}	Total applied current imposed through the tab (A)
A_{tab}	Geometric area of the tab where I_{app} is applied (m²)
n_{e}	Number of electrons transferred per electrochemical reaction step

1. CHAPTER I – INTRODUCTION

This chapter presents the general context of the research, the addressed problem and the objectives of the project. It serves to situate the reader within the theoretical and applied framework of the work.

1.1 Context and motivation

Lithium–ion batteries have transformed energy storage for consumer electronics, electric vehicles and renewable–energy infrastructures because they combine high energy density with long service life. The rapid electrification of transport, large–scale deployment of wind and solar generation, and society's appetite for ever more powerful portable devices have made electrochemical storage a strategic pillar of economic growth and decarbonization [1]. According to Figure 1.1 with the market analyses offered by Benchmark Mineral Intelligence, a private firm specializing in the lithium–ion battery supply chain, project that cumulative demand for lithium-ion batteries will exceed 3 TWh/year by 2030, more than doubling today installed manufacturing capacity [2]. This rapid growth brings three intertwined challenges: boosting energy density and cycle life to drive down the levelized cost of storage, securing sustainable and traceable supply chains for anode–critical materials such as natural graphite, lithium, and battery–grade silicon while limiting mining impacts, and establishing efficient recycling and safe end–of–life disposal pathways to close the materials loop and curb long–term ecological risks.

A rechargeable cell is based on the joint work of the cathode, the anode and the electrolyte. The cathode sets the upper voltage limit, the electrolyte shuttles Li^+ while preventing short–circuit, and the anode stores Li^+ during charge. Continued incremental improvements in layered–oxide cathodes are approaching the transition–metal redox ceiling, whereas liquid electrolytes have already undergone extensive optimization for safety and conductivity. By contrast, the negative electrode retains considerable untapped capacity, making it the most promising lever for next–generation energy density [3].

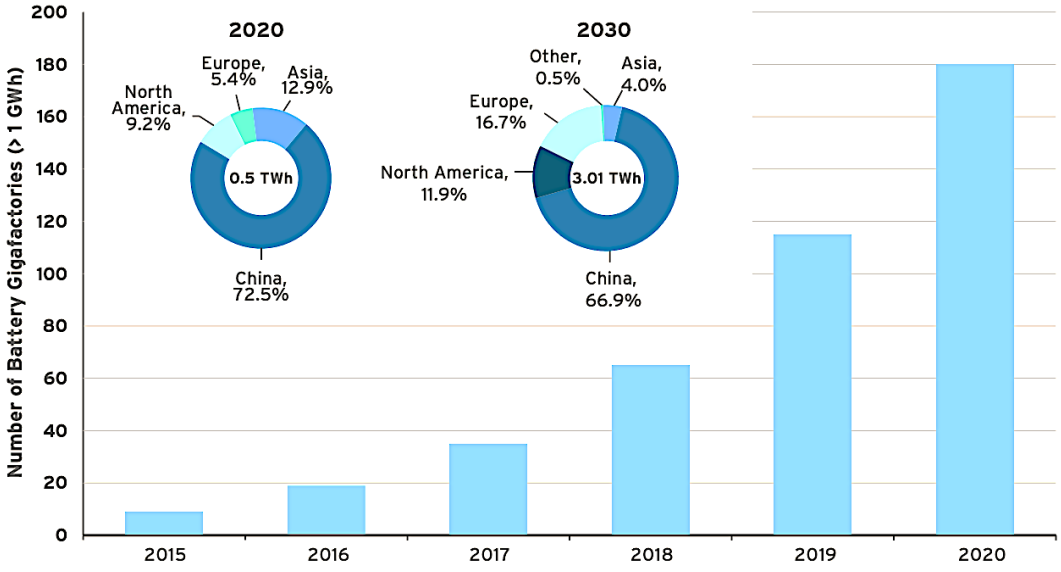

Figure 1.1. Battery gigafactory trend and regional market share [2].

Commercial anodes are still dominated by graphite, whose low intercalation potential, robust cycling behavior and well–documented stability make it an attractive, low–risk choice [4]. Nevertheless, the theoretical limit of 372 mAh/g now constrains long–range electric vehicles, rapid–charge applications and high–demand stationary systems; at the same time, the concentration of natural–graphite mining in a few geographical regions raises sustainability and geopolitical concerns [5]. These pressures have intensified research into alternatives that can deliver higher energy density through more efficient use of lithium–hosting materials without prohibitive penalties in cost or durability.

1.2 Challenges of next–generation batteries anodes

Several candidate materials have emerged to solve the above–mentioned problems. Silicon offers an exceptional theoretical capacity of about 3,579 mAh/g, an order of magnitude above graphite [6]. Unfortunately, silicon expands by almost 300 % during lithiation; that surge induces particle fracture, electronic disconnection, excess electrolyte consumption, and uncontrolled thickening of the solid–electrolyte

interphase (SEI) [7, 8]. Over the past decade researchers have attempted to tame these failures by shrinking silicon to the nanoscale, coating or doping its surface, and embedding it in hollow, porous, core–shell or yolk–shell structures [8, 9]. While each of these strategies has helped slow degradation, none has succeeded in preventing the gradual capacity loss caused by repeated SEI re–formation.

A complementary strategy that has gained attention involves embedding conductive materials, such as carbon black, graphite, graphene, and carbon nanotubes, into Si–based composites to address these constraints [10]. These composites partially stabilize the SEI, enhance electron transport, and reduce mechanical stresses cause by volume fluctuations [11]. For instance, Si/C composites made by pyrolyzing carbon precursors or high–energy milling show superior cycling stability compared to pure Si [10]. Similarly, adding graphene or carbon nanotubes to nanosized silicon improves conductivity and facilitates expansion; yet even sophisticated materials are still unable to completely eradicate SEI reformation and progressive capacity loss [12].

Considerable progress has also been reported by companies aiming to commercialize silicon–enriched anodes for greater energy density, improved longevity, and faster charging. NanoGraf's SiOx/graphene anodes promise 20 % extra range and ten–fold faster charging, though at higher cost [13]. ProLogium embeds SiOx in solid–state lithium–ceramic batteries to remove flammable electrolytes and block dendrites, but high ceramic cost, SiOx integration challenges and poor ionic conductivity below 0 °C remain hurdles [14]. Amprius, spun out of Stanford, has showcased silicon–nanowire cells at ~450 Wh/kg with an 80 % recharge in six minutes: yet nanowire fabrication cost, mechanical swelling and automotive–scale production cap adoption [15, 16].

Metallic lithium itself provides the ultimate anode limit of 3,860 mAh/g and the lowest electrochemical potential, enabling cell specific energies beyond 400 Wh/kg, but dendrite growth and unstable solid–electrolyte interphases currently hinder commercial deployment [17]. $Li_4Ti_5O_{12}$ (LTO) sacrifices energy density for a virtually "zero–strain" framework that delivers up to ten–thousand stable cycles and outstanding safety under fast–charge and low–temperature conditions [18], hard

carbon extends capacity to the 250–350 mAh/g range while improving low–temperature and high–rate capability relative to graphite [19].

On the other hand, advanced carbon–based nanostructures such as doped or functionalized carbon nanotubes (CNTs), carbon nanofibers (CNFs), heteroatom–doped graphene and three–dimensional porous carbon offer high lithium storage capacities, often exceeding 700 mAh/g [20]. Their curved, hollow, or multi–shell architectures help buffer volume changes during lithiation and enhance conductivity. However, their complex synthesis routes, high production costs, and limited scalability remain key obstacles for widespread industrial application.

Overall, each of these materials excels in one or two performance metrics yet carries intrinsic trade–offs in volumetric expansion, dendrite risk, cost or first–cycle efficiency. Consequently, it is imperative to explore anode architectures that boost specific capacity without sacrificing stability or inflating the cost structure.

1.3 Multilayer anode architectures: Chronological survey of key developments

Building on the preceding discussion about physicochemical advantages of graphite, silicon, LTO, graphene-derived carbons and other hosts, the following narrative traces year by year how researchers progressively combined those constituents into vertically-stacked multilayer anodes (Figure 1.2).

Within the first proofs of concept, it is possible to find in 2014, when Choi et al. confined nano-LTO between a graphene current-collector and an outer SWCNT film, sustaining 109 mAh /g at 100 C for 1 000 cycles and revealing that carbon cladding can buffer oxide expansion while supplying electronic pathways [21].

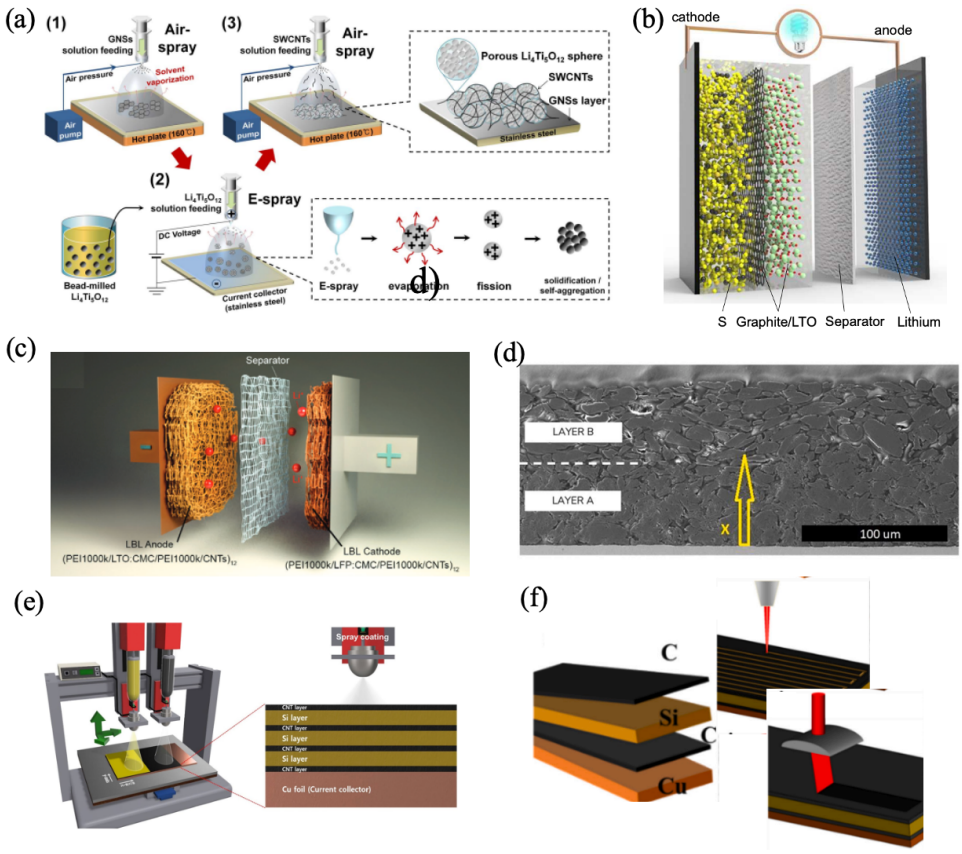

Figure 1.2. Representative multilayer electrode architectures explored in recent studies, including: (a) Nano–LTO aggregates confined between graphene and SWCNT networks [21], (b) A hybrid lithium–sulfur battery where a sulfur–rich electrode (90 wt% S–10 wt% Super P) is covered by graphite and LTO layers [22], (c) A full lithium–ion cell integrating multilayered anode and cathode architectures self–assembled via electrostatic interactions within a 3D porous melamine foam substrate [23], (d) A multilayer anode with vertically graded porosity dense near the current collector and open near the separator developed by EnPower Inc. [24], (e) A multilayer Si/CNT anode fabricated via ultrasonic spray coating with alternating conductive and active layers [25], and (f) A graphite/Si–rich multilayer anode featuring femtosecond–laser–engraved micro–channels to enhance electrolyte access and cycling stability [26].

Two years later, the focus shifted to lithium-metal systems. Lin et al. showed that layered reduced-graphene-oxide (rGO) with sub-10 nm gaps guides uniform Li deposition for >1 000 cycles at 3–5 mA/cm² [27]. The same year, Ming et al. stacked a S/graphite/LTO tri-layer that delivered 572 mAh/g with 82 % retention after 100 cycles and using a water–based binder, proving that electrochemically complementary layers can be combined without complex binders [22]. Extending the rGO strategy, Bai et al. (2018) spray-coated graphene-oxide sheets that spontaneously reduce to a ~330 nm film an optimum thickness that suppresses dendrites yet preserves ionic resistance [28].

In 2017, Guo et al. explored layer–structured materials such as graphite and metal oxides using techniques like chemical/mechanical exfoliation, host molecule intercalation, and hydro/solvothermal synthesis to enhance reactivity, ion accessibility, and structural stability [29]. In the same year, Sharma et al. illustrated a cost-aware alternative, physically mixing hard-carbon with LTO cut lithium inventory by ~80 % yet preserved 500 full-cell cycles, underscoring that power-energy trade-offs can be tuned even without precise layering [30].

The following year, in 2018, Su et al. encapsulated each Si particle inside a 4–5 nm pyrolytic-carbon shell and an outer rGO skin, curbing ~300 % volume expansion and sustaining >2 000 mAh/g for 200 cycles, though initial coulombic efficiency remained <80 % [23]. To achieve greater control over the electrode architecture, Wang et al. (2020) adopted electrostatic layer-by-layer self-assembly, sequentially depositing conductive carbon and Li-intercalating oxide nano-bilayers. The resulting electrodes exhibited 28 % lower charge-transfer resistance than slurry-cast controls, confirming that ordered stacks can outperform mixed slurries when interfacial coherence is critical [31].

In 2023, Hamedi et al. work with graded porosity vertically, dense near the current collector, open near the separator to enable 5 C charging without Li plating, a design commercialized by EnPower Inc. and retaining >80 % capacity after 500 cycles [24]. Complementary laser-printed laminates from Rist et al. exposed the danger of

under-engineered binders, graphite /Si (12 wt %)/graphite stacks failed prematurely when PVDF could not absorb Si swelling. At the same time, Müller et al. mapped how Si content and particle size govern calendaring response, giving a quantifiable window for multilayer thickness optimization [32].

Ko et al. (2024) alternated three Si sheets with CNT networks via ultrasonic spray-coating; the laminated cell retained 157.6 mAh/g after 500 cycles at 2 A/g, while reducing charge-transfer resistance and boosting the Li^+ diffusion coefficient to 1.19×10^{-13} cm^2/s, yet MWCNT cost still clouds industrial feasibility [25]. Finally, Yuan et al. (2025) demonstrated a graphite/Si-rich composite graphite sandwiches whose top layer was micro-channeled with a femtosecond laser. After 300 cycles it still delivered 1 350 mAh/g, 40 % above a nano-Si benchmark validating the dual strategy of graphite-buffered SEI formation and inner-Si high capacity [26].

Taken together, these studies chart a trajectory from early carbon–buffer concepts to today's porosity–graded, micro–machined stacks, as multilayer anodes converge on three recurring principles. First, an outer carbonaceous layer that stabilizes the SEI. Second, an inner layer with high gravimetric capacity, shielded from direct electrolyte contact. Third, mechanical or porosity gradients that buffer the stresses induced by fast charging. The simulation framework developed in this thesis follows the same model, positioning a pure graphite surface layer over a second layer, either pure or composite, adjacent to the current collector; this configuration harnesses the high gravimetric capacity and the added stability provided by the second material.

Despite these advances, designers still lack a quantitative framework that links layer thickness, material choice, and porosity to energy density, impedance growth, and cycle life. Most published studies are empirical and difficult to compare, which slows industrial scale–up. This thesis fills that gap with a physics–based, statistically driven simulation workflow that maps the multilayer–anode design space and provides clear guidelines for building high–energy, long–life lithium–ion cells.

1.4 Objectives

1.4.1 General Objective

Develop quantitative guidelines for multilayer lithium–ion battery anode design via COMSOL Multiphysics® electrochemical simulations and JMP® statistical analysis, to identify optimal graphite buffer and second–layer configurations (graphite–silicon and alternative materials) that maximize specific capacity and cycling stability without significantly increasing cost or manufacturing complexity.

1.4.2 Specific Objectives

1. Determine the silicon content and bilayer thickness ratio that maximize capacity retention and minimize SEI–induced degradation in a graphite + Si–graphite anode after 2 000 cycles at 1C.
2. Identify the three most promising second–layer materials among hard carbon, lithium titanate (LTO), silicon and lithium metal composites for enhanced long–cycle performance.
3. Quantify the ohmic resistance (R_s), SEI + charge–transfer resistance (R_{SEI} + R_{ct}) and Warburg coefficient of the top five cell simulated.
4. Benchmark the optimized cells against literature and commercial references to extract practical design guidelines for multilayer anodes.

2. CHAPTER 2 – METHODOLOGY OF MULTILAYER ANODE MODELING

2.1 Hypothesis and variable selection

The initial hypothesis suggests that adding an outer graphite layer in direct contact with the electrolyte will act as both a mechanical and electrochemical buffer, protecting the inner graphite–silicon layer. This graphite layer will reduce direct silicon–electrolyte exposure, decreasing SEI formation and thickness, lowering electrolyte consumption during cycling, and smoothing overpotential spikes. As a result, the silicon can provide its high capacity without affecting the cell's structural integrity or stability.

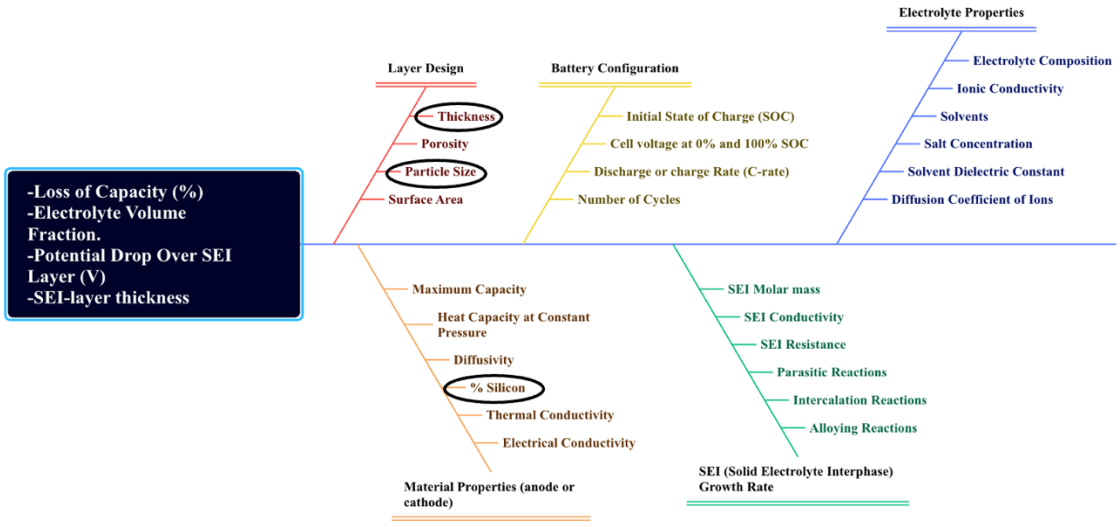

Figure 2.1. Fishbone diagram of factors influencing degradation mechanisms in multilayer anodes.

Once the null hypothesis is established, the next step is to identify the variables in the factorial design that directly impact the critical degradation mechanisms observed in multilayer silicon–graphite anodes (Figure 2.1). Attention first turned to the electrolyte–facing graphite layer, whose surface area dictates the initial Li^+ flux and

SEI growth kinetics. Three complementary studies (Bläubaum et al., 2020 [33]; Gottschalk et al. [34], 2024; Luo et al., 2024 [35]) converge on the idea that keeping the median graphite particle diameter below ≈ 9 µm suppresses overpotential and plating while preserving tap density and mechanical cohesion.

The silicon–rich secondary layer markedly increases capacity but also induces severe volumetric expansion. Although multilayer architectures were addressed earlier, two studies warrant renewed attention. Rist et al. (2023) evaluated a graphite/Si/graphite laminate containing 12 wt % Si. Müller et al. (2023) varied the Si fraction from 0 to 15 wt % and the particle diameter from 120 to 250 nm, recording the best performance at the smaller size. They further demonstrated that a thin carbon overcoat suppresses degradation only when the Si content remains close to 10 wt %. Complementary mechanical tests by Geng et al. (2024) found that pure–Si layers thicker than 40 µm delaminate within 200 cycles, whereas 10–20 µm layers remain mechanically stable [36].

These results delineate practical boundaries that inform the proposed COMSOL–JMP optimization: First, confine Si to 10–30 wt % with a strong bias toward the 10–15 wt % range and use nano–Si (<120 nm) to limit pulverization; second, keep individual active layers ≤ 20 µm and total anode stacks ≤ 60 µm to balance diffusion paths and mechanical integrity; lastly, integrate a conductive buffer graphite with a particle size of up to 9 µm.

Other variables from the diagram were fixed or excluded to maintain computational feasibility. The cathode and the electrolyte were held constant across all simulations to isolate the effects of anode design. The baseline chemistry NMC 622 as cathode, 1 M $LiPF_6$ in EC/EMC (3:7) as electrolyte, and Cu/Al current collectors was chosen because each component simultaneously advances energy density, reliability, and manufacturing practicality. The Ni–rich composition of NMC 622 pushes the

reversible capacity well beyond that of lithium–iron–phosphate while retaining better thermal stability than cobalt–rich LCO; at the same time, its trimmed cobalt content lowers raw–material cost and sidesteps many of the ethical concerns linked to Co mining [37]. That higher capacity pairs naturally with silicon–enhanced anodes, enabling the full cell to exploit silicon's volumetric and gravimetric advantages without being bottlenecked at the cathode.

The EC/EMC solvent blend, fixed at a 3:7 proportion, unites the high dielectric constant of ethylene carbonate which promotes a stable solid–electrolyte interphase with the lower viscosity of ethyl methyl carbonate, thereby enhancing ionic transport at low temperature. $LiPF_6$ remains the preferred conducting salt because its broad electrochemical stability window and fluorophosphate decomposition products passivate internal surfaces [38]. Copper and aluminum current collectors contribute reliable conductivity and corrosion resistance, ensuring that insights from the simulated parameter sweeps can be transferred directly to scalable pouch–cell prototypes without extensive redesign [39].

Temperature was maintained at 25 °C to avoid introducing non–linear thermal dependencies. Additionally, material properties such as density, conductivity, and specific heat were treated as constants based on standard literature values. These simplifications allowed the simulation to focus on structural parameters that are both practically controllable and strongly correlated with battery degradation pathways.

Finally, grounding the factorial design within these experimental validated registers, the project could rapidly simulate parameter combinations and alternative second layer materials with high confidence that the simulated optima will translate into durable and high energy multilayer anodes suitable for potential scalability.

2.2 Phase I: Optimizing a Graphite + Graphite-Silicon bilayer

COMSOL Multiphysics® was used to simulate the electrochemical behavior of lithium–ion cells with multilayer anodes. According to Figure 2.2, these simulations explored different silicon ratios in the composite layer, the graphite particle size and diverse layer thicknesses of Graphite/Graphite+Silicon. The total thickness was maintained at 60 μm, a constraint that simplified computational demands, mitigated lithium transport limitations, and reduced capacity losses at high charge/discharge for a potential pouch cell.

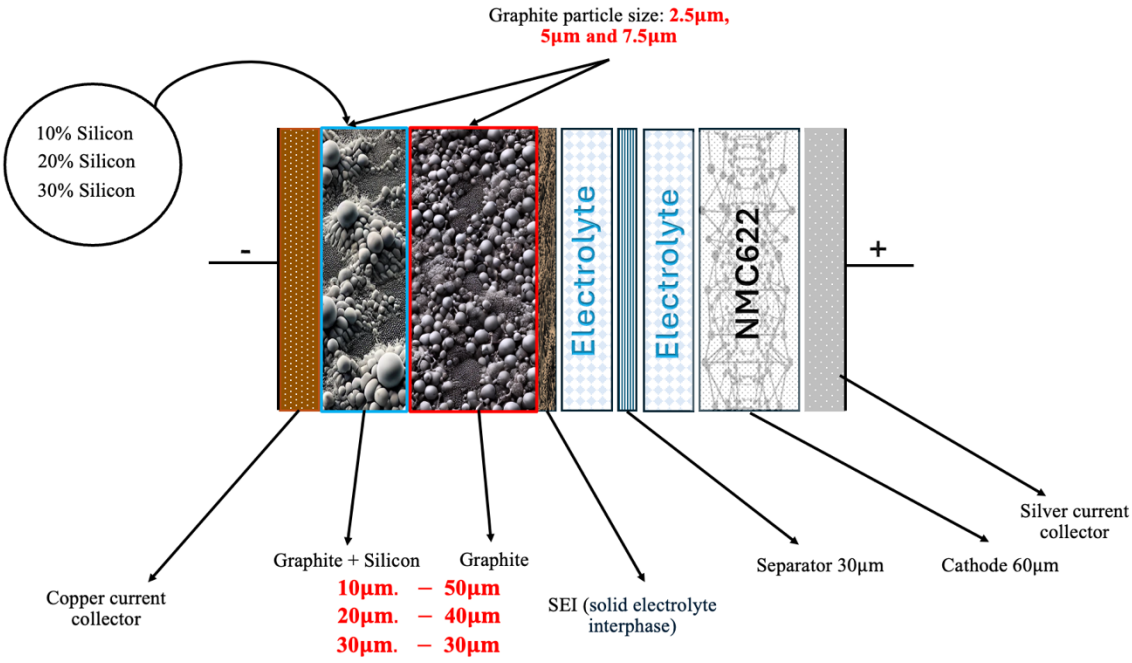

Figure 2.2. Schematic representation of battery that will be modeled in the Phase 1.

After 2 000 charge discharge cycles at 1 C, four responses are extracted: SEI potential drop (mV), relative capacity retention (%), SEI thickness (μm), residual electrolyte volume fraction.

A full 3^3 factorial design was constructed, resulting in twenty–seven distinct simulation runs. The study systematically varied three key input factors, each at three

levels, thereby exhaustively exploring the design space most relevant to degradation and performance in multilayer lithium–ion battery anodes. This experimental structure ensured that both main effects and potential interactions among the variables could be identified with statistical rigor.

All data processing was performed in JMP®, where multivariate analysis of variance quantified the individual contributions of each factor and their second–order interactions across the four response variables of interest. Prediction profilers were then developed to visualize how each response evolved throughout the simulated parameter space, revealing inflection points, nonlinear behaviors, and critical thresholds.

Finally, a desirability–function analysis combined the four responses into a single composite index. Specific goals were assigned to each response and JMP calculated the global desirability surface. The peak of this surface identified the operating configuration that offered the best overall trade–off between performance and durability.

2.3 Phase II: Exploring alternative materials for the second layer

From first phase, two important parameters are extracted: the graphite particle size to be used as the buffer layer (the layer in direct contact with the electrolyte), and the layer thicknesses that demonstrated the best diffusion and stability. Once these parameters are determined, the graphite-Si composite is replaced by three active phases hard carbon (H), lithium titanate oxide (LTO) and lithium metal (ML) each tested both in its pure form (100 %) and as 10/20/30 wt % composites with graphite (Figure 2.3).

The identical 2000-cycle protocol yields directly comparable electrochemical and impedance metrics. Therefore, upon completion of all simulation run with twelve additional cases for the hard carbon, LTO and lithium–metal composites the three configurations exhibiting the highest overall performance will be identified, alongside the top silicon configuration from phase I and the baseline 100 % graphite reference.

For each of these five cells, the response metrics used in Phase 1 will be directly compared: SEI overpotential drop (mV), relative capacity retention (%), SEI thickness (µm), and electrolyte volume fraction.

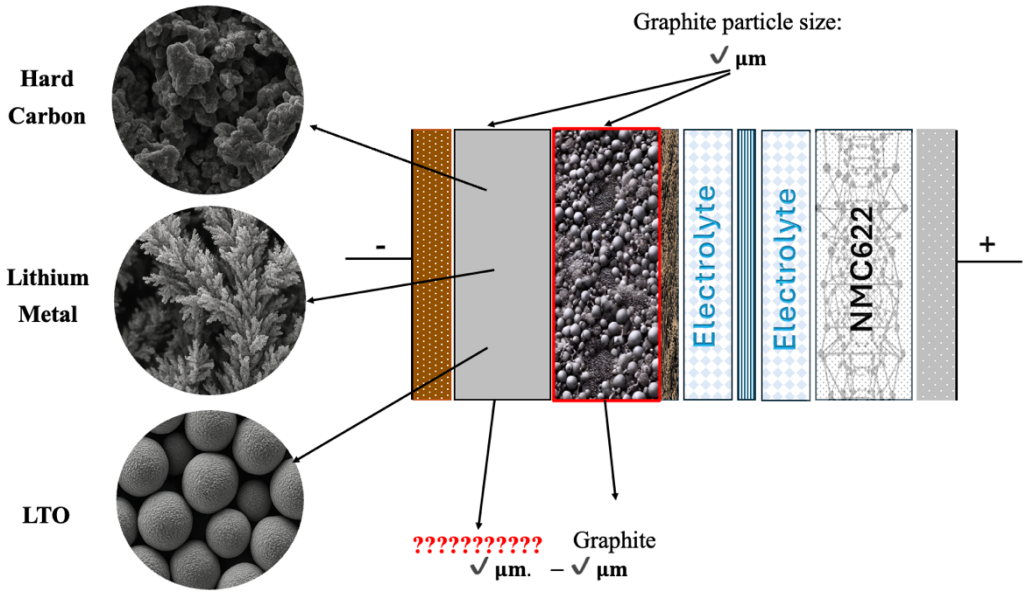

Figure 2.3. Schematic representation of battery that will be modeled in the Phase 2.

Subsequently, electrochemical impedance spectroscopy (EIS) will be carried out in COMSOL. First, Nyquist plots (–Z″ vs. Z′) will be generated to isolate electrolyte and contact resistance (R_s) at high frequencies and combine SEI plus charge–transfer resistance ($R_{SEI} + R_{ct}$) in the mid–frequency semicircles, while Bode plots of Z′ vs. frequency will show how total resistance shifts from electrolyte–dominated at high frequencies to diffusion–limited at low frequencies. Finally, plotting –Z″ vs. frequency separates capacitive from diffusive phenomena, a distinct peak or plateau at mid–frequencies indicate double–layer or SEI capacitance, while the characteristic −45° slope at low frequencies confirms Warburg–type diffusion [40]. Extracted values of R_{ct}, R_{SEI} and the Warburg coefficient will reveal which multilayer architecture best balance reaction kinetics, mechanical resilience and long–term capacity retention.

Finally, conclusions will be drawn based on the configurations that exhibited the most favorable results. These findings will be compared against reported composites or

multilayer configurations from the literature, and where appropriate, against commercially available batteries. This comparative analysis will serve to support and validate the initial hypothesis regarding the use of a protective graphite buffer layer as a potential solution for integrating high–capacity active materials without compromising stability or key performance properties over extended cycling.

2.4 Mathematical Model

This study models multilayer anodes comprising a first layer of graphite in direct contact with the electrolyte and a second layer made of a graphite–silicon mixture. The investigation evaluates how material properties and geometry (with varying thicknesses) influence the transport of species within the anode. The analysis focuses on lithium diffusion in the system, considering both intrinsic transport within each layer and transport across the interface between layers [41].

The ionic and electronic transport within the battery is described using the Bruggeman relation, which provides an expression for the effective ionic conductivity of the electrolyte. The effective conductivity κ_{eff} is given by [42]:

$$\boldsymbol{\kappa_{eff} = \kappa \cdot \epsilon^{brugg}} \quad \textit{Eq. 2.1}$$

In this equation, κ represents the intrinsic ionic conductivity of the electrolyte, defining how easily lithium ions can move through the liquid medium. The term ϵ refers to the porosity of the electrode, indicating the fraction of the volume available for ion transport. The parameter brugg, known as the Bruggeman coefficient, adjusts for the tortuosity of the porous medium, reflecting how the actual pathways for ion movement are longer and more complex than the straight–line distance due to the structure of the electrode. This relation is particularly important for multilayers anodes, where the porosity and tortuosity vary between layers, influencing the overall ionic conductivity.

The diffusion model utilized in this project for the multilayer anode is the Baker–Verbrugge [42], selected for its ability to accurately capture the complexities of

lithium–ion transport within active material particles in lithium–ion batteries. Unlike classical diffusion models such as Fick's Law, which assumes linear concentration gradients and constant diffusivity, the Baker–Verbrugge model incorporates the effects of spherical particle geometry and concentration–dependent diffusion. This makes it particularly suitable for simulating the non–linear behavior of lithium ions during intercalation and de–intercalation processes in multilayer anodes. The Baker–Verbrugge model addresses these limitations by integrating a spherical divergence operator, enhancing the model's capacity to predict real–world battery performance under various operating conditions [42, 43]:

$$\frac{\partial c_s}{\partial t} = \frac{1}{r^2}\frac{\partial}{\partial r}\left(D_{\text{eff}}\, r^2 \frac{\partial c_s}{\partial r}\right) \quad \textbf{Eq. 2.2}$$

In this equation, c_s represents the lithium concentration in the solid phase, expressed in mol/m³, which indicates the amount of lithium intercalated within the graphite particles. This concentration varies both temporally and spatially, reflecting the dynamic process of lithium insertion and extraction during charge and discharge cycles. The variable t , measured in seconds, denotes time and captures the evolution of the lithium distribution as the electrochemical reactions progress. The radial coordinate r, expressed in meters, represents the particle mean center–surface distance, which is essential for modeling the radial nature of lithium diffusion in spherical geometries.

The effective diffusion coefficient, D_{eff}, with units of m²/s, quantifies the ease with which lithium ions diffuse through the solid matrix simulated. Unlike the constant diffusion coefficients used in simpler models, can vary with factors such as lithium concentration, temperature, and the microstructural characteristics of the electrode material. The term $\frac{1}{r^2}\frac{\partial}{\partial r}\left(D_{\text{eff}}\, r^2 \frac{\partial c_s}{\partial r}\right)$ is the spherical divergence operator, which accounts for the changes in the surface area available for diffusion as lithium ions move radially. This operator ensures that the model accurately captures the non–linear distribution of lithium within the particle, reflecting real–world diffusion behavior.

The partial differential equation in Eq. 2.2 is closed by the following boundary conditions:

$$\left.\frac{\partial c_s}{\partial r}\right|_{r=0} = 0, \quad -D_{\text{eff}} \left.\frac{\partial c_s}{\partial r}\right|_{r=R_p} = \frac{i_{loc}}{F\,a} \quad \textit{Eq. 2.3}$$

The insertion of lithium ions into solid materials is a key process that directly impacts the performance of lithium–ion batteries. In this study, a multilayer anode structure is modeled, where the first layer is composed of graphite in direct contact with the electrolyte, while the second layer consists of a composite material made of graphite and silicon in varying proportions. The kinetics of lithium insertion, which govern the intercalation reaction at the electrode–electrolyte interface, are crucial in determining the behavior of these systems. The lithium insertion kinetics are modeled using the Butler–Volmer equation, which establishes the relationship between local current density and the electrochemical conditions at the interface [44]. This equation accounts for the dependence of the local current density on factors such as the exchange current density, the overpotential, and the transfer coefficients associated with the anodic and cathodic reactions. The local current density is mathematically represented as:

$$i_{loc} = i_0 \left(exp\left(\frac{\alpha_a F \eta}{RT}\right) - exp\left(-\frac{\alpha_c F \eta}{RT}\right)\right) \quad \textit{Eq. 2.4}$$

Here, i_0 represents the exchange current density, η denotes the overpotential, and α_a and α_c are the anodic and cathodic transfer coefficients, respectively. The exchange current density, i_0 ,characterizes the intrinsic reaction kinetics and depends on the lithium concentration in both the solid phase and the electrolyte. The calculation of the exchange current density is expressed as:

$$i_0 = i_{0,\text{ref}} \left(\frac{c_s}{c_{s,\max}}\right)^{\alpha_c} \left(1 - \frac{c_s}{c_{s,\max}}\right)^{\alpha_a} \left(\frac{c_l}{c_{l,\text{ref}}}\right)^{\alpha_a} \textit{Eq. 2.5}$$

Here c_s denotes the local lithium concentration in the active particle, $c_{s,\max}$ its maximum storage capacity, c_l the local Li^+ concentration in the electrolyte, and $i_{0,\text{ref}}$ the reference exchange–current density defined at the electrolyte concentration $c_{l,\text{ref}}$.

The first factor in Eq. 2.5 accounts for the fraction of occupied intercalation sites, the second for the fraction of vacancies, and the third introduces the electrolyte dependence.

Charge conservation is fundamental in electrochemical systems, ensuring that the total charge within the battery remains balanced. For the solid phase, which includes the electrode materials, charge conservation is expressed as:

$$\boldsymbol{\nabla \cdot i_s = -a \cdot i_0} \quad \textit{Eq. 2.6}$$

Here, i_s represents the current density in the solid phase, while a denotes the specific surface area of the electrode, which influences the rate of electrochemical reactions. The current density i_s is also related to the potential in the solid phase through Ohm's law:

$$\boldsymbol{i_s = -\sigma_s \nabla \phi_s} \quad \textit{Eq. 2.7}$$

In this expression, σ_s is the electrical conductivity of the solid material, indicating how effectively electrons can move through the electrode. The potential gradient $\nabla\phi_s$ drives the flow of electrons, and this relationship is crucial for modeling the electronic behavior within each layer of anode.

The conservation equation in Eq. 2.7 is solved subject to:

$$\boldsymbol{\phi_s|_{\Gamma_{Cu}} = 0}, \qquad \boldsymbol{n \cdot i_s|_{\Gamma_{Al}} = -\frac{I_{app}}{A_{tab}}} \quad \textit{Eq. 2.8}$$

Where Γ_{Cu} and Γ_{Al} denote the boundary surfaces in contact with the negative (copper) and positive (aluminum) current collectors, respectively; and $n \cdot i_s$ represents the normal component of the electronic current density crossing the boundary.

In the electrolyte phase, charge conservation is described by a similar equation:

$$\boldsymbol{\nabla \cdot i_l = a \cdot i_0} \quad \textit{Eq. 2.9}$$

Here, i_l represents the ionic current density in the electrolyte. The expression for i_l incorporates both migration and diffusion contributions [45]:

$$\boldsymbol{i_l = -\kappa_{eff}\nabla\phi_l + \kappa_{eff}\frac{RT}{F}(1 - t^+)\nabla \ln c_l} \quad \textit{Eq. 2.10}$$

In this equation, ϕ_l is the electrolyte potential, and t^+ is the transference number of lithium ions, the term c_l is the concentration of lithium ions in the electrolyte, R, T and F, are the universal gas constant, temperature, and Faraday's constant, respectively. The first term represents the ionic migration due to the electric field, while the second term accounts for diffusion driven by concentration gradients.

On electrically insulated or symmetry boundaries such as the lateral pouch edges what ensuring that no ionic or electronic current leaves the domain through those surfaces, the following condition applies:

$$\boldsymbol{n \cdot i_l = 0, \quad n \cdot i_s = 0.} \quad \textit{Eq. 2.11}$$

Mass conservation is another critical aspect, ensuring that the transport of lithium ions within the battery is accurately represented. In the electrolyte, mass conservation is described by:

$$\boldsymbol{\epsilon\frac{\partial c_l}{\partial t} = \nabla \cdot \left(D_{eff}\nabla c_l\right) + \frac{1-t^+}{F} a \cdot i_{loc}} \quad \textit{Eq. 2.12}$$

The first term on the right–hand side represents the diffusion of lithium ions due to concentration gradients, while the second term accounts for the generation or consumption of lithium ions because of electrochemical reactions at the electrode–electrolyte interface.

The stoichiometric reaction of lithium insertion involves the intercalation of lithium ions and electrons into vacant reaction sites within the solid material. This process is expressed as: $\mathrm{Li}^+ + e^- + \Theta \leftrightarrow \mathrm{Li}\Theta$, where Θ represents the vacant reaction sites, and $\mathrm{Li}\Theta$ indicates the occupied sites. The concentration of vacant sites is related to the total capacity of the material and the current concentration of lithium as:

$$\boldsymbol{c_\Theta = c_{max} - c_s} \qquad \textit{Eq. 2.13}$$

To evaluate the state of charge (SOC) of the electrode, a dimensionless parameter is introduced to quantify the fraction of occupied sites:

$$SOC = \frac{c_s}{c_{max}} \qquad \textbf{Eq. 2.14}$$

From a mathematical perspective, the flow of ions through each layer depends on concentration gradients and diffusion coefficients, if the first layer is too thin for example, 10 μm of graphite followed by 50 μm of a graphite–silicon mixture lithium ions from the electrolyte must pass through a very narrow graphite region before reaching the thicker, silicon–rich layer. This setup puts significant strain on the thin graphite layer to supply ions to the larger second layer, intensifying concentration gradients and local current density (Eq. 2.4). As a result, higher overpotentials and polarization occur, which limit how effectively the silicon layer can be utilized because the thinner graphite layer simply can't supply ions quickly enough.

This issue is not only evident in theory but also becomes apparent when simulating these configurations using COMSOL Multiphysics®. Models with an excessively thin first graphite layer frequently failed to converge on a solution because it reflects an unfeasible or electrochemically unstable design. This numerical instability aligns with the mathematical explanation: poorly balanced layer thicknesses create physical conditions that are difficult to manage and computationally challenging to simulate, reinforcing the need for a more balanced design.

On the other hand, when the thickness of the graphite layer is closer to that of the silicon–containing layer such as 30 μm of graphite paired with 30 μm of graphite–silicon, or 40 μm with 20 μm the internal conditions of the anode enable a smoother and more manageable ion flow. This balance results in gentler concentration gradients, lower overpotentials, and stable simulations. The outcome is better ion distribution, improved silicon utilization, and enhanced overall stability for the anode.

In summary, both the mathematical analysis and the numerical evidence from COMSOL Multiphysics® highlight the critical importance of properly balancing the thickness ratios in multilayer anode designs. A well–thought–out configuration

prevents bottlenecks, optimizes electrochemical performance, and ensures that modeling and simulations provide accurate and reliable results.

2.5 Electrochemical reactions in Lithium–Ion battery systems

The formation of the SEI layer is modeled using equations that describe the reactions and processes occurring at the anode (Table 2.1). In this case, the multilayer anode consists of a pure graphite layer directly in contact with the electrolyte, where SEI formation takes place, and a secondary layer made of a graphite–silicon mixture, which serves exclusively as a lithium–ion storage medium. While this secondary layer does not participate directly in SEI formation, its higher storage capacity can influence the electron demand of the graphite layer. By varying the thickness of the graphite layer (30, 40, and 50 μm), the study examines how resistance and the kinetics of electrochemical reactions are impacted.

The local current density driving SEI formation on the graphite surface is expressed by the equation:

$$\boldsymbol{i_{loc,\,SEI} = -(1 + H_k)\frac{J i_{loc,\,1C,\,ref}}{exp\left(\frac{\alpha \eta_{SEI} F}{RT}\right) + \frac{q_{SEI} f J}{i_{loc,\,1C,\,ref}}}} \quad \textbf{Eq. 2.15}$$

In this equation, H_k is the graphite expansion factor that depends on the state of charge (SOC), J is the exchange current density for the parasitic reaction, α is the transfer coefficient of the electrochemical reduction reaction, η_{SEI} represents the overpotential for SEI formation in volts, q_{SEI} is the local accumulated charge due to SEI formation in coulombs per square meter and f is a lumped parameter related to the SEI film properties with units of 1/s. Finally, $i_{loc,\,1C,\,ref}$ corresponds to the reference current density for a 1C charge. The parameters, H_k, J and α varies depending on the percentage of silicon to be evaluated.

The lumped film parameter f serves as a key approximation for cumulative SEI growth during extended cycling. The numerical values assigned to f, H_k, J and α were selected from standard benchmarking studies and tuned in COMSOL to mimic real–world battery aging behaviour.[46]. The values are pre–defined to balance accuracy with computational efficiency, ensuring that key phenomena are well–captured without overcomplicating the model.

The model also accounts for the coupling between different active materials, such as Graphite and Graphite + Silicon in the negative electrode. This coupling is achieved by defining separate diffusion coefficients and Butler–Volmer kinetics for each material and combining their effects based on their respective volume fractions. The total current density in the negative electrode is expressed as:

$$\boldsymbol{i_{loc,\,SEI} = f_G \cdot i_G + f_{G+S} \cdot i_{G+S}} \qquad \textbf{\textit{Eq. 2.16}}$$

Here, f_G and f_{G+S} are the volume fractions of graphite and graphite + silicon, respectively, while i_G and i_{G+S} represent the current local densities associated with SEI each material. This formulation allows the model to capture the distinct electrochemical behaviors of different active materials and their combined contribution to the overall battery performance.

The temporal evolution of SEI concentration is modeled by:

$$\frac{\partial c_{SEI}}{\partial t} = \frac{\nu_{SEI} i_{loc,\,SEI}}{n_e F} \qquad \textbf{\textit{Eq. 2.17}}$$

Here, c_{SEI} represents the accumulated SEI concentration on the anode, ν_{SEI} is the stoichiometric coefficient of the reaction product, and n_e is the number of electrons transferred per reaction.

The SEI thickness, δ_{film}, increases as the reaction progresses and is calculated as:

$$\boldsymbol{\delta_{film} = \frac{c_{SEI} M_{SEI}}{A_v \rho_{SEI}} + \delta_{film,0}} \qquad \textbf{\textit{Eq. 2.18}}$$

where $M_{\mathrm{SEI}}$is the molar mass of the reaction product, A_v is the effective surface area and ρ_{SEI} is the density of the solid product and $\delta_{\mathrm{film},0}$ is the initial SEI thickness.

The resistance associated with the SEI is calculated as:

$$\boldsymbol{R_{film} = \frac{\delta_{film}}{\kappa_{film}}} \qquad \textbf{\textit{Eq. 2.19}}$$

Where κ_{film} is the SEI's conductivity, additionally, the resistance increases as the SEI layer thickness, affecting the anode's electrochemical performance.

The primary chemical reaction for SEI formation is $S + \mathrm{Li}^+ + e^- \rightarrow P_{\mathrm{SEI}}$, where S represents the electrolyte solvents (e.g., ethylene carbonate) and $P_{\mathrm{SEI}}$is the solid reaction product. To accelerate aging simulations, a time factor is introduced, modifying the reaction as $\tau S + \mathrm{Li}^+ + e^- + (\tau - 1)\mathrm{Li(s)} \rightarrow \tau P_{\mathrm{SEI}}$, where $\tau = 250$ is ideal as it strikes a balance between computational efficiency and physical accuracy. This setting ensures that each simulated cycle corresponds to 250 real cycles, reducing computation time while still providing realistic predictions of capacity fade, SEI growth, and resistance changes.

Table 2.1 lists the electrochemical reactions that including lithium intercalation in graphite and hard carbon, silicon alloying, lithium plating/stripping, LTO redox, as well as secondary SEI formation and impurity-driven pathways each classified by reaction type. However, only the primary intercalation and alloying reactions under standard charge/discharge conditions were implemented in the COMSOL Multiphysics® simulations to ensure that the model faithfully reproduces the active anode behavior without incorporating secondary or anomalous processes.

Table 2.1. Summary of Electrochemical Reactions.

Name	Formula
Reversible Silicon Alloying	$Si + xLi^+ + xe^- \rightarrow Li_xSi$
Lithium Intercalation in Graphite	$C + xLi^+ + xe^- \rightarrow Li_xC_6$
Delithiation of NMC622 Cathode	$LiNi_{0.6}Mn_{0.2}Co_{0.2}O_2 \rightarrow Ni_{0.6}Mn_{0.2}Co_{0.2}O_2 + Li^+ + e^-$
Formation of Dilithium Ethylene Dicarbonate	$2C_3H_4O_3 + 2Li^+ + 2e^- \rightarrow (CH_2OCO_2Li)_2 + C_2H_4$
Formation of Lithium Carbonate and Ethylene	$C_3H_4O_3 + 2Li^+ + 2e^- \rightarrow Li_2CO_3 + C_2H_4$
Reduction of Ethyl Methyl Carbonate (EMC) to form Methyl Lithium Carbonate and Ethane.	$OC(OCH_3)_2 + 2Li^+ + 2e^- \rightarrow LiCH_3OCO_2 + C_6H_6$
Formation of Lithium Carbonate and Methane from EMC	$OC(OCH_3)_2 + 2Li^+ + 2e^- \rightarrow Li_2CO_3 + CH_4 + C_2H_6$
Formation of Lithium Alkyl Carbonates	$OC(OCH_3)_2 + Li^+ + 2e^- \rightarrow LiOCO_2R + R'$
Hydrolysis of PF_6^-	$PF_6^- + H_2O \rightarrow POF_3 + 2HF$
Water Reduction on Graphite Anode	$2H_2O + 2e^- \rightarrow H_2 + 2OH^-$
Formation of Lithium Hydroxide	$Li^+ + OH^- \rightarrow LiOH$
Decomposition of Ethylene Carbonate with Water	$C_3H_4O_3 + H_2O \rightarrow C_2H_6O_2 + CO_2$
Reaction of Dissolved CO_2 with Lithium	$CO_2 + 2Li^+ + 2e^- \rightarrow Li_2CO_3$
Global Reaction: Metallic Lithium	$Li(s) + e^- \rightarrow Li(s)$
Global Reaction: LTO (Lithium Titanium Oxide)	$Li_4Ti_5O_{12} + 3\,Li^+ + 3\,e^- \rightarrow Li_7Ti_5O_{12}$
Global Reaction: Composite (10% Si, 90% Graphite)	$0.1\,Si + 0.9\,C_6 + 1.34\,e^- + 1.34\,Li^+ \rightarrow 1.34\,(Li_xSi) + LiC_6$
Global Reaction: Hard Carbon	$HardC + Li^+ + e^- \rightarrow Li(HardC)$
Global Reaction: Silicon	$Si + 4.4\,Li^+ + 4.4\,e^- \rightarrow Li_{4.4Si}$

3. CHAPTER 3 – RESULTS AND DISCUSSION

This chapter presents and discusses the results obtained from the two simulation phases detailed in the methodology. Phase I (Section 3.1) optimizes the graphite/graphite–silicon bilayer via a 3^3 full–factorial design that varies silicon content, graphite particle size and layer–thickness ratio. Four key responses such as capacity fade, SEI thickness, SEI overpotential and electrolyte consumption are analyzed to pinpoint the most balanced configuration. Phase II (Section 3.2) carries forward the optimal particle size and thickness ratio from Phase I, replacing the inner layer with hard carbon, lithium titanate oxide (LTO) or metallic lithium at various weight fractions. The same electrochemical responses are evaluated, and impedance spectroscopy (R_s, $R_{SEI} + R_{ct}$, Warburg coefficient) is added to compare kinetics and durability. Together, these results validate the hypothesis that a fine–particle graphite buffer decouples SEI formation from internal kinetics, providing quantitative guidelines for high–energy multilayer anode design.

3.1 Phase 1 results and discussion

Phase 1 of the simulation design was implemented using JMP software to systematically assess the influence of three key input factors on cell performance: layer configuration, particle size, and silicon percentage. Each factor was varied at three distinct levels, leading to a 3^3 full factorial design and resulting in a full factorial set of 27 simulated runs. Layer configuration involved three thickness distributions for the double–layer anode (for example, 30–30 μm, 20–40 μm, and 10–50 μm), particle size was varied at three different diameters (2.5 μm, 5 μm, and 7.5 μm), and the silicon content in the graphite–silicon composite layer was tested at 10%, 20%, and 30%. This setup allowed a structured exploration of the design space, with the goal of identifying which input factors most significantly affect the critical response variables.

The responses under investigation were percentage of capacity loss(%), thickness of the SEI layer (μm), potential drop across the SEI layer (mV), and the fraction of electrolyte consumed after 2,000 cycles. These responses were selected based on a detailed analysis of the parameters that most directly influence battery longevity and

energy density. By varying the three main input factors across all 27 simulated runs, the design provided a robust method of Multivariate analysis of variance (MANOVA) for identifying how magnitude and behavior of each factor's impact on the responses, as shown in Figure 3.1, with individual results reported in Table 3.1.

The JMP Effect Summaries and accompanying ANOVA tables show that reports in Figure 3.1 are statistically significant, that is, their interactions fall below significance level $\alpha = 0.05$. This shows that all the variables under consideration silicon content, particle size, and layer configuration along with certain factor combinations, have a statistically significant impact on the response. Adjusted R^2 values ranging from 0.74 to 0.97 confirm that the models explain most of the observed variability. Therefore, choosing these variables as simulation factors is both appropriate and well–founded, and variations in any of them can directly affect cell stability and performance.

The hierarchy of influence shifts by response: capacity fade is driven chiefly by Si %, followed by the configuration × Si interaction; SEI thickness is dominated by particle size; potential drop is governed by particle size and layer configuration; and electrolyte consumption is once again highly sensitive to Si %. This behavior highlights the multi-objective nature of the problem no single factor can be optimized in isolation, because its impact is conditioned by how it couples with the others.

Table 3.1. Simulation results by battery configuration.

Layer configuration : xx–yy (µm) = inner | outer layer	Graphite Particle Size (µm)	Silicon (%)	Loss capacity (%)	SEI layer thickness (µm)	Potential drop over SEI layer (mV)	Electrolyte consumed (%)
30–30	5	10	14.1	0.49	86.3	26.8
20–40	**2.5**	**30**	**17.5**	**0.49**	**46.7**	**53.9**
20–40	7.5	10	22.6	1.34	187.2	34.2
30–30	7.5	20	17.4	0.96	63.3	35.5
20–40	5	20	15	0.76	104.9	41.3
10–50	7.5	20	24.2	1.2	241.1	44.5
30–30	7.5	30	22.7	1.4	83.1	51.8
10–50	5	10	14.1	0.64	177.6	34
20–40	5	30	17	0.97	77.9	52.8
30–30	2.5	10	14.2	0.25	49.2	27.5
30–30	2.5	30	23.1	0.48	34.9	53.3
20–40	5	10	16.4	0.62	150.6	33
30–30	**2.5**	**20**	**18.4**	**0.34**	**31.6**	**37.5**
10–50	2.5	30	15	0.5	89	52.5
10–50	2.5	20	14.1	0.37	75.1	38.9
10–50	7.5	30	24.4	1.57	221.4	55.3
30–30	5	30	23.2	0.95	68.7	53.2
10–50	5	30	17.2	1.03	179.4	54.3
10–50	2.5	10	12.4	0.3	63.5	33
10–50	5	20	16.1	0.77	191.4	40.6
20–40	2.5	10	14.6	0.3	76.6	31.7
30–30	7.5	10	13.8	0.69	104.7	25.5
20–40	2.5	20	14.9	0.55	60.2	42.3

Table 3.1. Final simulation results by battery configuration (Continuation).

Layer configuration	Graphite Particle Size (µm)	Silicon (%)	Loss capacity (%)	SEI layer thickness (µm)	Potential drop over SEI layer (mV)	Electrolyte consumed (%)
20–40	7.5	30	16.4	1.4	84.7	50.9
10–50	7.5	10	18.4	1	235.1	35.3
20–40	7.5	20	15.1	1.01	125.4	39.6
30–30	5	20	18.1	0.67	53.7	36.9
100% Graphite	**2.5**	**N/A**	**7.09**	**0.2536**	**59.3**	**42.88**
100% Graphite	5	N/A	8.78	0.2452	238	44.77
100% Graphite	7.5	N/A	12.16	0.2367	557.3	46.69
90% Graphite – 10% Silicon	**2.5**	**10**	**16.00**	**0.59**	**152.1**	**62.73**
90% Graphite – 10% Silicon	5	10	37.23	1.37	672.4	71.78
90% Graphite – 10% Silicon	7.5	10	70.35	1.36	985.2	47.36
80% Graphite – 20% Silicon	2.5	20	100	0.93	1410	1

With these models validated (global model $p < 0.0001$ in every ANOVA), the next step in JMP is to build the composite desirability function. Based on these goals, one can scan design space for the factor combination that maximizes overall desirability. The resulting desirability plot provides a data driven candidate for the optimal configuration; this setting will then be subjected to higher-fidelity simulations or prototype testing, scaling on the experimental design cycle.

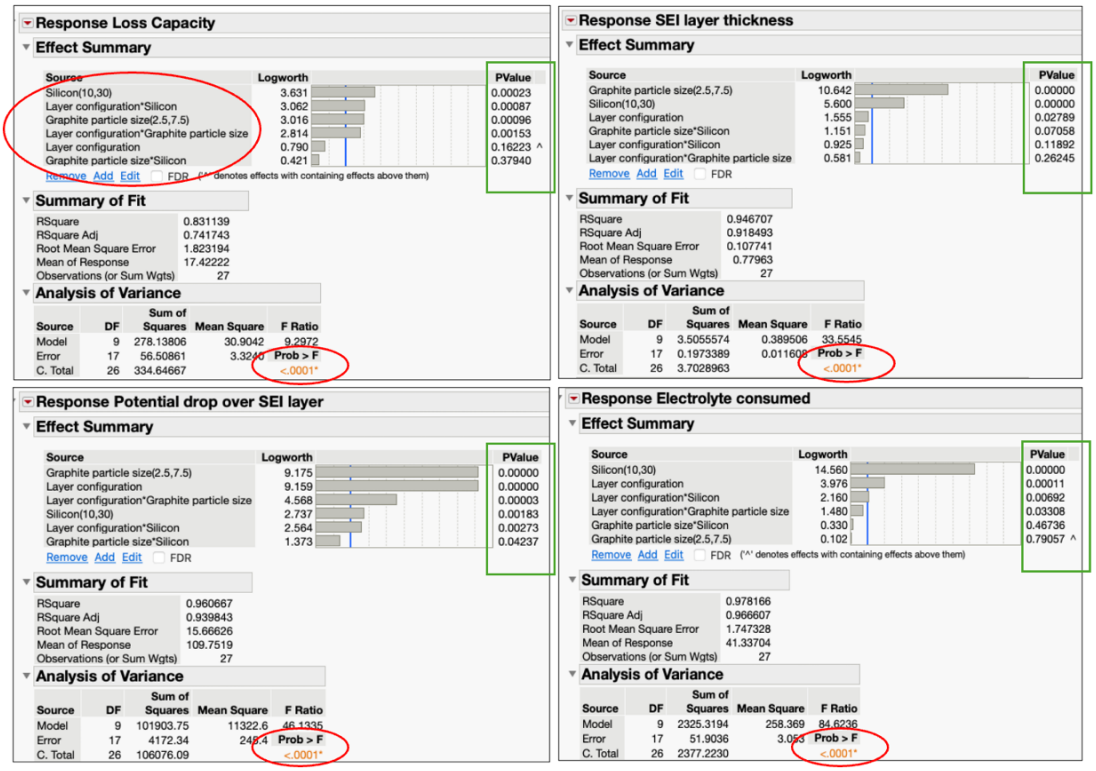

Figure 3.1. JMP effect and ANOVA summaries for the four battery–performance metrics.

Additionally, Figure 3.3 shows the prediction profiles clearly illustrate how the responses shift as each factor level is adjusted. From these profiles, it becomes evident that the condition of highest instability arises when combining the most critical levels, for instance, a higher silicon content, a change in layer thickness or a specific particle size. Additionally, these profiles make it possible to estimate confidence intervals shown as gray bands or bracketed values in blue, providing a more accurate sense of the variability in each response. At this setting the model predicts a capacity loss of 20.0 % (95 % CI 17.9–22.1 %), a SEI thickness of 0.36 µm (0.25–0.46 µm), a potential drop across the SEI of 41.9 mV (23.5–59.8 mV), and electrolyte consumption of 43.7 % (41.7–46.7 %) after 2 000 simulated 1 C cycles.

Finally, the maximum desirability reported indicates that the 30–30 µm configuration, with a 2.5 µm particle size and 23.07% silicon content, yielded the best results according to the statistical prediction. This result surpasses the optimal monolayer mixture reported by Ambrock et al. (2023), which consisted of 85% graphite and 15% silicon with nanostructured silicon particles [47]. However, for comparative purposes, the 30–30 µm design with a 2.5 µm particle size and 20% silicon was selected and

compared with an equivalent composite battery design featuring the same proportional percentage of silicon, specifically a monolayer battery composed of 90% graphite and 10% silicon. Additionally, it is important to note that the maximum desirability of the battery was calculated based on standard values from conventional graphite batteries that utilized the same materials for the remainder of the battery. A second design, 20–40 µm with a 2.5 µm particle size and 30% silicon, was included in the comparative model because it exhibited results close to the maximum desirability and maintained the same silicon proportion. Finally, the four simulated prototypes were simulated under the same global dimensions and input conditions to calculate the response variables and perform the analysis.

This statistical analysis, combined with a factorial design approach, ensures that the selected levels for each factor and their interactions are grounded in objective and reproducible quantitative data. Consequently, before moving to model validation, it becomes possible to identify the parameter combinations that lead to the most severe degradation, as well as to determine the optimal design strategies to mitigate battery aging.

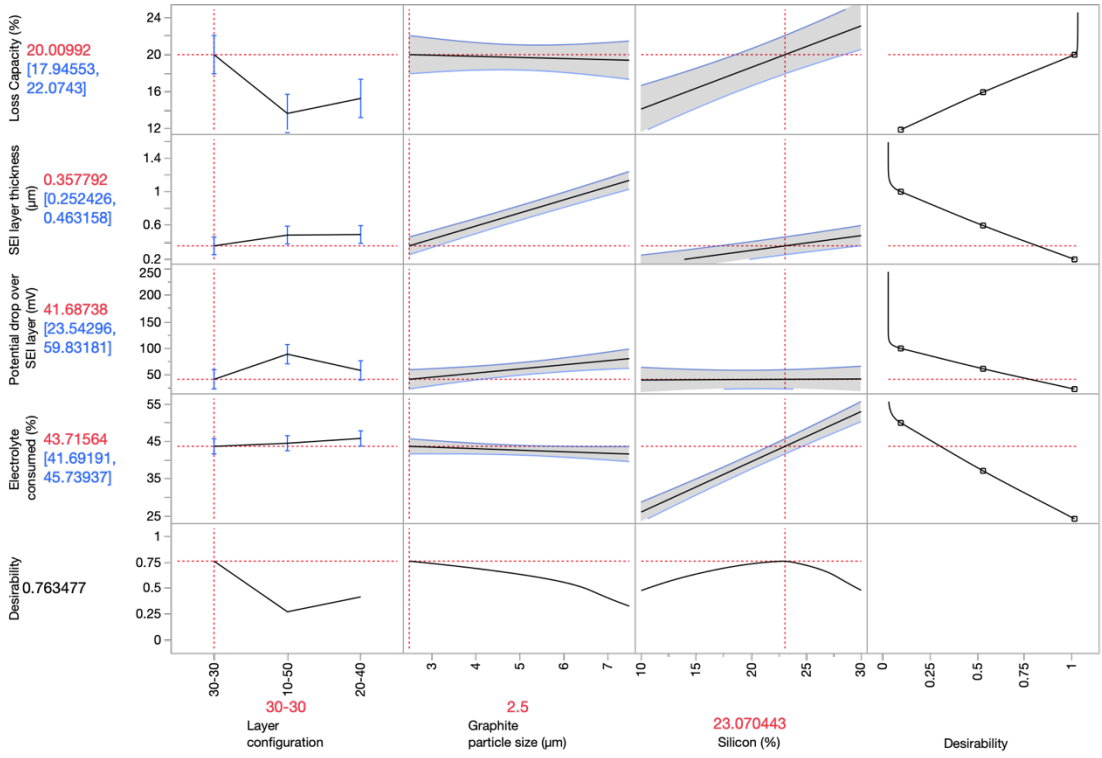

Figure 3.2. Prediction profiler developed in JMP to maximize desirability.

When comparing these configurations in Figure 3.3, the 100% graphite battery exhibits the lowest capacity loss (~7%), an electrolyte consumption of approximately 43%, and an SEI thickness of 0.42 μm. The potential drop reaches 59.3 mV, indicating that, in terms of capacity retention, this formulation is highly stable. However, the incorporation of silicon even in moderate amounts leads to an increase in storage capacity at the expense of introducing adverse effects. In fact, the monolayer configuration consisting of 90% graphite and 10% silicon undergoes a degradation of ~16%, accompanied by a pronounced potential drop (152 mV), higher electrolyte consumption (62.7%), and the formation of a thicker SEI (0.59 μm). In other words, while silicon enhances the effective capacity, it also intensifies the mechanisms of electrolyte consumption and SEI growth.

In the multilayer configurations of 30–30 μm and 20–40 μm, the capacity loss is approximately 18.4% and 17.5%, respectively, which are slightly higher than those observed in the monolayers. However, their advantages in terms of electrochemical stability are evident: the electrolyte consumption (38% and 54%) is lower than that of the silicon–containing monolayer, and the SEI thickness (0.34 and 0.49 μm) remains below that of the monolayer. Furthermore, the potential drop for the 30–30 configuration 31.6 mV is considerably lower than that of the silicon or graphite monolayer, while in the 20–40 configuration it rises to 92.8 mV, a value still below the 152 mV observed in the silicon monolayer. These findings suggest that employing a relatively thick first layer of graphite coupled with a second layer incorporating silicon mitigates the direct exposure of silicon to the electrolyte, thereby reducing overpotential spikes and enhancing anode safety [23].

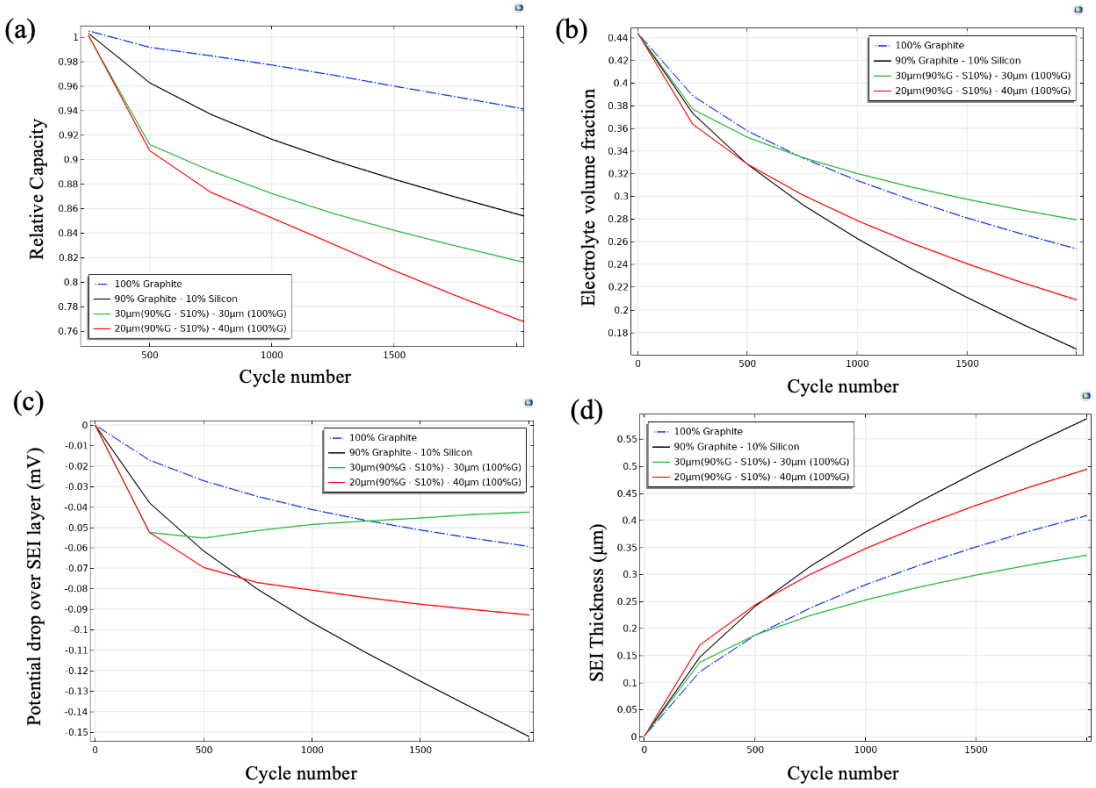

Figure 3.3. Comparative evolution of capacity (a), electrolyte volume fraction (b), potential drop over the SEI (c), and SEI thickness (d) in four different anode configurations over cycling in a 1D pouch battery. The SEI–related voltage loss in (c) is plotted as a negative quantity to reflect its subtractive effect on terminal voltage.

In a 100% graphite anode, the minimal capacity fade is largely due to graphite's inherent stability and reduce volumetric expansion. However, pure graphite exhibits a relatively higher potential drop, which can be attributed to its less efficient ion transport and the formation of a comparatively thicker, resistive SEI layer when directly exposed to the electrolyte. In contrast, the 30–30 configuration presents an advantage, although the inclusion of silicon induces a higher degradation due to its significant volumetric expansion and associated mechanical stress, the outer graphite layer serves as an effective buffer. This protective layer minimizes direct contact between the reactive silicon and the electrolyte, reduce the formation of a thicker resistive SEI, ensures a more uniform current distribution and enhanced electronic conductivity. Consequently, the 30–30 design achieves a significantly lower potential drop despite the slightly increased capacity fade. This engineered architecture thus

leverages the high capacity of silicon while mitigating its adverse effects on interfacial resistance, resulting in improved overall electrochemical performance.

It is interesting to note that the simulation model includes a configuration with a 50 μm thick graphite layer and a 10 μm thick graphite–silicon layer, which exhibits the lowest deterioration approximately 12.4% capacity fade. Previous studies on monolayer systems, such as those by Raić (2023), have demonstrated that increasing the thickness of silicon–based electrodes can impede lithium–ion diffusion and result in higher internal resistance accelerating capacity fade due to mechanical stress and unstable SEI formation [48]. However, this comes at the expense of having such a small fraction of silicon that the overall capacity of the anode does not increase significantly; furthermore, as shown in Table 3.1, the electrochemical properties are more sensitive to increases in the silicon percentage in thin layers. This result reveals that having a substantially thicker graphite layer than the graphite–silicon layer optimizes current distribution and minimizes the ionic transport bottleneck, thereby reducing degradation. Moreover, underscore the importance of maintaining an appropriate balance between layer thickness and the silicon proportion used to mitigate the adverse effects of silicon incorporation and avoid ionic transport issues and excessive concentration gradients that would otherwise accelerate system degradation.

Regarding electrolyte consumption, Figure 3.3b shows that the configuration where the mixture (90% graphite and 10% silicon) has silicon in direct contact with the electrolyte exhibits the worst results in terms of electrolyte consumption. This is consistent with previous reports, such as those by Wang et al. (2022), where insufficient electrolyte volume caused by solvent depletion during SEI growth can significantly accelerate capacity loss and shorten the cycle life of lithium–ion batteries [44]. However, the bilayer configurations showed the best results, with the 30–30 configuration performing the best.

Figure 3.4 shows the State of Charge (SOC) profiles of four anode configurations after 2,000 cycles at 1C. The double–layer configurations exhibit a steeper SoC rise in the initial phase, indicating relatively rapid charge acceptance during early charging. In

contrast, the single–layer anode with 90% graphite and 10% silicon shows a more gradual SoC progression, likely due to the direct exposure of silicon to the electrolyte and the resulting formation of thicker SEI layers. Meanwhile, the 100% graphite anode maintains a stable, continuous increase, reflecting its lower internal resistance. Comparing earlier to later cycles reveals that the silicon–containing anodes' curves tend to diverge, indicating higher degradation, whereas the pure–graphite configuration remains relatively stable. Overall, while silicon contributes additional capacity, it also introduces more complex kinetics; the double–layer arrangement mitigates direct silicon–electrolyte interactions and helps balance the electrochemical performance over extended cycling.

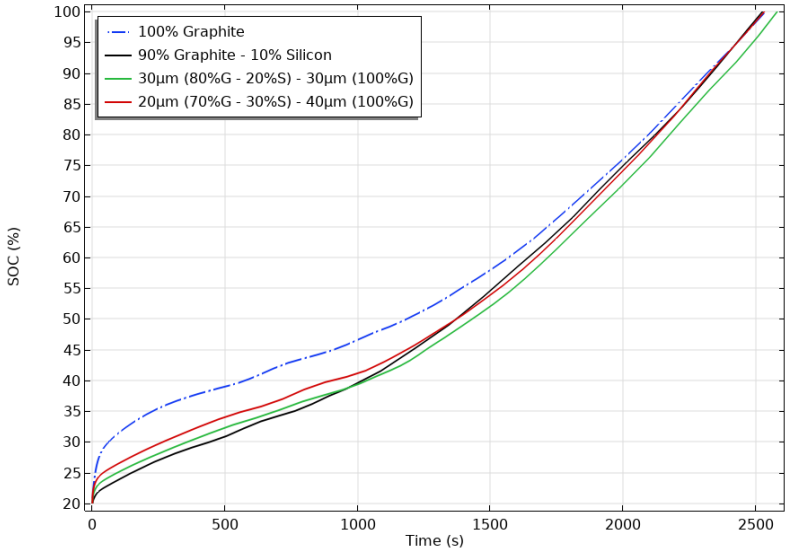

Figure 3.4. SOC evolution during charging for different anode configurations simulated in a 3D pouch battery.

All four curves start from the same state of charge (SOC) of 20%, as recommended by Horstkötter and Bäker (2023) to minimize storage degradation [49]. However, they begin at different voltage points due to variations in the chemistry and morphology of each anode. Even when the overall silicon proportion is the same in three of the anodes, the layered configuration (e.g., 30 µm/30 µm vs. 20 µm/40 µm) modifies the current distribution and internal resistance across the electrode. This variation in resistance and the lithium–ion circulation path leads to slight misalignments in the starting voltage, which are not strictly tied to the initial state of charge.

In prior research, Andersen et al. (2019) investigated the performance of silicon–carbon composite anodes using industrial–grade silicon for batteries [50]. Their findings revealed behavior like the results of this study, particularly in the voltage–capacity relationship, but with significantly lower charging efficiency. Their configuration utilized a homogeneous mixture of silicon and graphite in direct contact with the electrolyte, which likely contributed to the reduced efficiency. This comparison underscores the advantages of the multilayer configuration proposed in the present work. By avoiding direct contact between the silicon–containing layer and the electrolyte, this design achieved a significant improvement in charge efficiency and overall performance, demonstrating the effectiveness of this approach in addressing the limitations observed in previous studies.

Figure 3.5 tracks how each anode design ages over 2 000 simulated discharge cycles. Every colored trace is a snapshot of the cell voltage at a given cycle number: blue corresponds to the first cycles, red to the last. In the 100 %–graphite reference (panel b), all traces lie almost perfectly on top of each other down to ~3.3 V, and only then begin to spread. This tight overlap indicates that the electrode resists degradation for a long portion of the discharge; the gradual widening below 3.3 V signals the onset of higher internal resistance as the solid electrolyte interphase (SEI) thickens. A similar pattern is observed in the layered electrodes of panels a and d, but the overlap persists slightly further down to ~3.2 V thanks to the protective graphite layer that moderates current density before lithium reaches the silicon-rich sub–layer. In contrast, the homogeneous 90 % G – 10 % Si electrode (panel c) shows noticeable separation from the start: each successive cycle drops more steeply than the previous one, reflecting faster impedance growth and uneven lithiation caused by silicon being exposed along the full thickness.

The plateau that develops between ~3.05 V and 2.9 V reveals when the silicon begins to release lithium. In the single–layer composite (panel c) this region is broad and shifts downward with cycling, confirming that silicon contributes capacity but also introduces larger overpotentials as its kinetics slow and mechanical strain accumulates. When silicon is confined to an interior band (panels a and d), the same plateau appears

later in the discharge and remains narrower, showing that the graphite shell helps distribute current, limit local stresses and keep the SEI growth under control. Consequently, the layered designs combine higher usable capacity with a more stable voltage profile over time, whereas the homogeneous composite gains capacity at the cost of accelerated polarization and earlier voltage collapse.

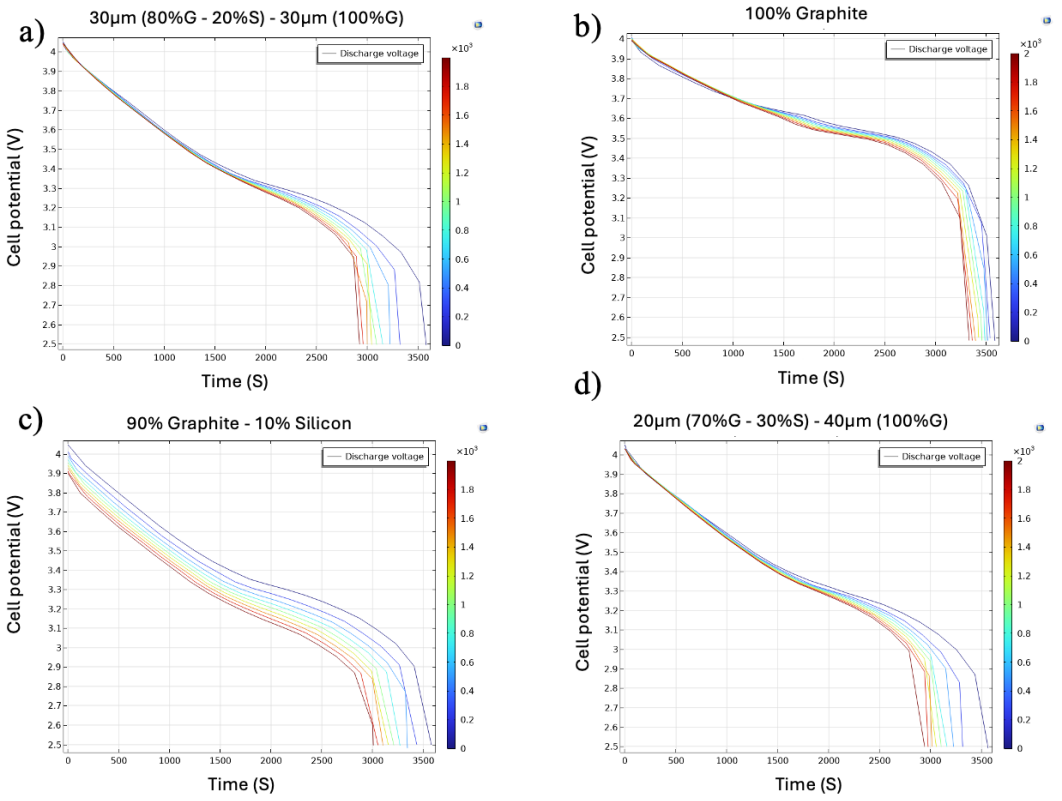

Figure 3.5. Cell potential evolution during discharge for (a) 30µm (90%G – 10%S) – 30µm (100%G), (b) 100% Graphite, (c) 90% Graphite – 10% Silicon, and (d) 20µm (90%G – 10%S) – 40µm (100%G).

During charge and discharge, graphite can reach very low potentials, approaching or even falling below the critical threshold (e.g., near 0 V versus Li/Li^+). In these extremely negative potential ranges, parasitic reactions intensify, promoting the formation and growth of a dense and unstable SEI layer. In contrast, when a second layer is introduced, as in the 30–30 configuration, the electrochemical behavior changes substantially. The outer graphite layer operates in a less extreme potential range, avoiding the aggressive drops that drive intense parasitic reactions. In this way, excessive SEI formation at the main interface is limited. The SEI layer thicknesses

shown in the Figure 3.6a corroborate this analysis, as the 30–30 configuration exhibits a much thinner SEI layer compared to the other configurations. This is a key point, as a thinner SEI layer implies lower electrolyte consumption and a more stable interface, which coherently explains the superior results obtained in the simulation for the 30–30 architecture [51].

On the other hand, the particle size is crucial for controlling porosity, ion diffusion, and the development of SEI. Therefore, understanding how to improve this parameter was fundamental to this study, as graphite constitutes the largest fraction of the anode, and its variability on an industrial scale is significant [52]. Figures 3.6 shows that smaller graphite particles, when combined with moderate silicon levels, generally result in lower potential drop over SEI layer at negative electrode–separator, in contrast, larger particles of 7.5 μm paired with a 30% silicon content exhibit significantly higher resistance.

As the graphite particle size increases, more pronounced voltage drops are observed across all anode configurations. This phenomenon stems from the augmented diffusion limitations and elevated internal resistance that accompany larger particles, culminating in higher polarization during charge and discharge cycles. Moreover, with larger particle sizes, the surface–area–to–volume ratio decreases, reducing the available reactive surface and thereby exacerbating the overpotential required to sustain a given current. Consequently, anodes composed of larger graphite particles tend to exhibit steeper voltage profiles and greater overall potential drops.

Several studies support these observations regarding the influence of particle size, Luo et al. (2024) tested particles of 6.5, 9.6, and 14.6 μm, finding that increasing size increases the likelihood of local Li^+ accumulation and reduces the anode's effective capacity [35]. Bläubaum et al. (2020) likewise investigated 1.53, 5.86, and 17.45 μm particles, concluding that smaller fractions perform better under high charge rates, whereas larger particles suffer greater kinetic losses and encourage lithium plating, leading to cracks in the electrode material [33].

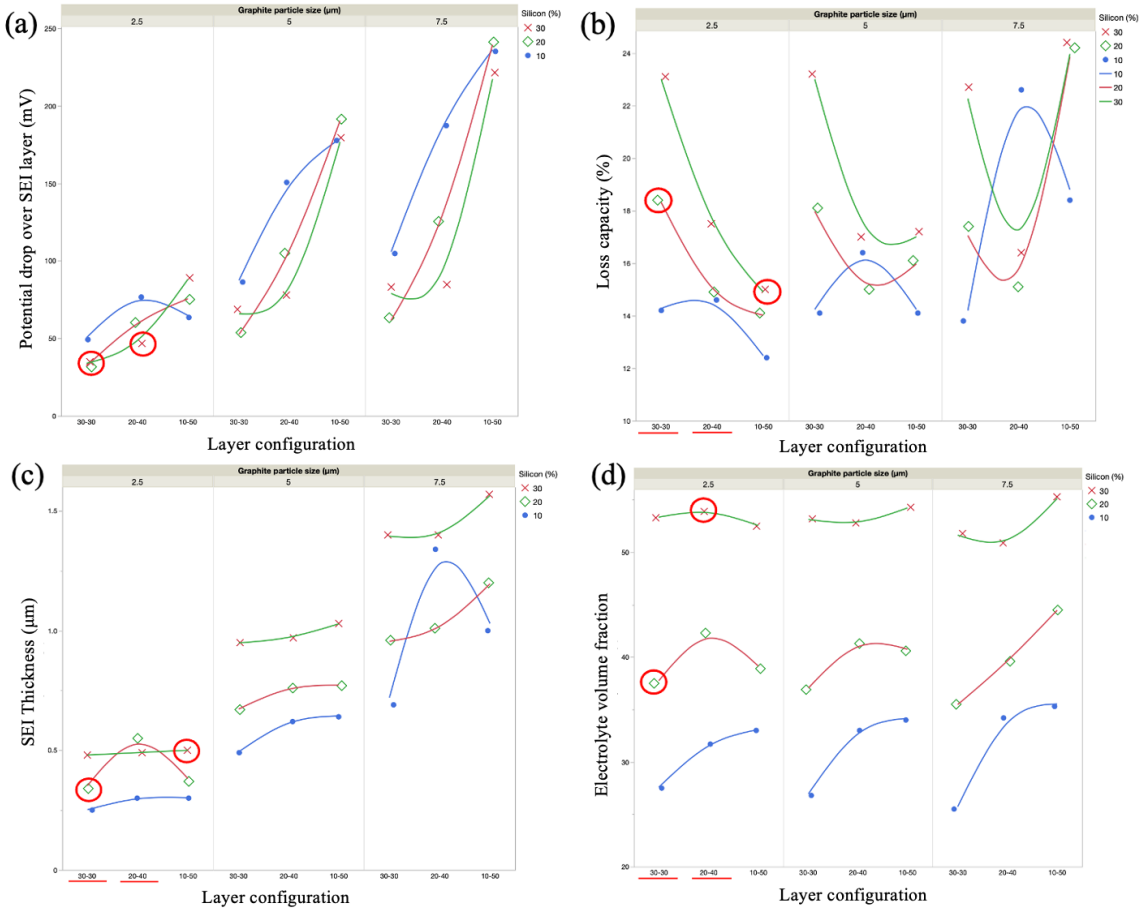

Figure 3.6. (a) Potential drop over the SEI layer at the negative electrode–separator interface as a function of particle size, layer configuration, and silicon content. (b) Loss in capacity under the same conditions. (c) SEI layer thickness evolution. (d) Electrolyte consumption trends.

Additionally, bigger particle sizes can offer certain advantages, as demonstrated by Gottschalk et al. (2024), who examined single– and double–layer anodes with particles of 18 and 11 µm [34]. Placing the larger particles in the layer adjacent to the electrolyte increased porosity and improved ion transport, while the smaller–particle layer contributed additional capacity without raising internal resistance. Overall, this dual–layer arrangement resulted in a more stable performance over cycling. Lastly, although Wan et al. (2023) focused on $LiFePO_4$ cathodes, their findings on how particle size impacts porosity and transport kinetics also apply to anodes. In both cathodes and anodes, the process of ion de–intercalation and the need to strike the right balance between porosity and active material loading are critical for ensuring low ionic resistance and high capacity [53].

Although this simulated study is favored by a small particle size due to the nature of the proposed materials, that small graphite particles, which tend to yield lower porosity, are not inherently detrimental or that large particles, which often provide greater porosity, automatically beneficial. Each particle size presents its own set of advantages and challenges, affecting both the transport of ions through the pores and the diffusion of lithium within the active material. The overall electrode performance depends on balancing factors such as diffusion length, reactive surface area, effective porosity, and overpotential. Furthermore, the importance of electrode architecture is highlighted and how strategies in the size particle and order of layers can enhance ion transport and capacity. Ultimately, these findings emphasize that optimal performance is achieved through the integrated control of microstructure, which reduces costs and experimental time.

In the contour plots of Figure 3.8, the interactions between the two continuous numerical variables graphite particle size and silicon percentage are illustrated for a fixed 30–30 configuration. With silicon content and graphite particle size as the primary tuning parameters, these plots reveal how the system's performance varies. Graph (a) shows the capacity trend, indicating that capacity increases with a decrease in particle size and an increase in silicon content, up to an optimal level where the benefits of higher theoretical capacity are balanced against the risks of excessive side reactions. Graph (b) presents the SEI layer thickness, demonstrating that smaller particle sizes combined with moderate silicon percentages (around 20 %) help to minimize SEI growth, preserving the interfacial stability.

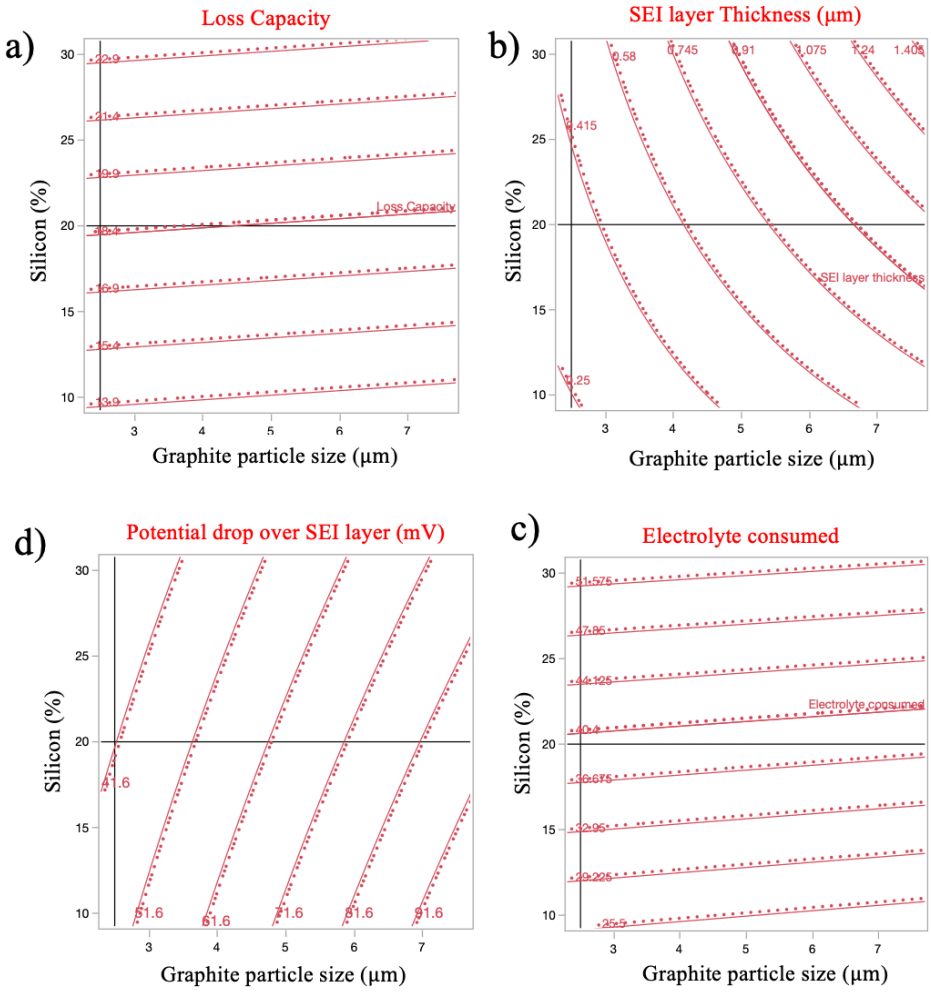

Figure 3.7. Contour Plots of (a) Capacity, (b) SEI Layer Thickness, (c) Potential Drop, and (d) Electrolyte Consumption for the 30–30 Multilayer Anode (20% Si, 2.5 µm Graphite Particles).

Graphs (c) further detail the electrochemical behavior depicts the potential drop over the SEI layer, where lower overpotentials are achieved under conditions of reduced particle size and moderate silicon, thus ensuring efficient electron transport, while graph (d) illustrates electrolyte consumption, which remains within acceptable limits when employing the 2.5 µm particle size and a 20 % silicon level. These trends correlate with the results and discussion section of the article, which emphasizes that the 30–30 configuration with 20 % silicon and 2.5 µm graphite particles provides an optimal balance, maximizing capacity while controlling SEI formation, potential drop, and electrolyte depletion. Consequently, this operating region is best positioned as the ideal performance zone for the multilayer anode design, ensuring enhanced energy density and extended cycle life.

1.1 Phase 2 results and discussion

The long–term performance of lithium–ion anodes depends critically on both the active–material composition and the interfacial reactions that occur during cycling. In particular, the formation and growth of the solid electrolyte interphase (SEI) consume lithium and electrolyte, leading to capacity loss and rising internal resistance with increasing cycle number. To probe these effects, five multilayer anode configurations were simulated in COMSOL Multiphysics using an NMC cathode, $LiPF_6$ in EC:EMC (3:7) liquid electrolyte, at room temperature and a 1C charge rate, over 2 000 cycles (Figure 3.8). Additionally, graphite particle size and layer thickness were defined based on the first phase of the project: a graphite particle diameter of 2.5 µm and an equal layer ratio (50:50), here represented as two 30 µm–thick layers. Particle sizes for the other materials were chosen according to bibliographic recommendations, hard carbon: 2.5 µm [54, 55]; lithium titanate (LTO):0.2 µm [56]; metallic lithium: 0.5 µm [57, 58]; and silicon: 0.1 µm to ensure realistic diffusion and interfacial behavior in each layer [9, 59]

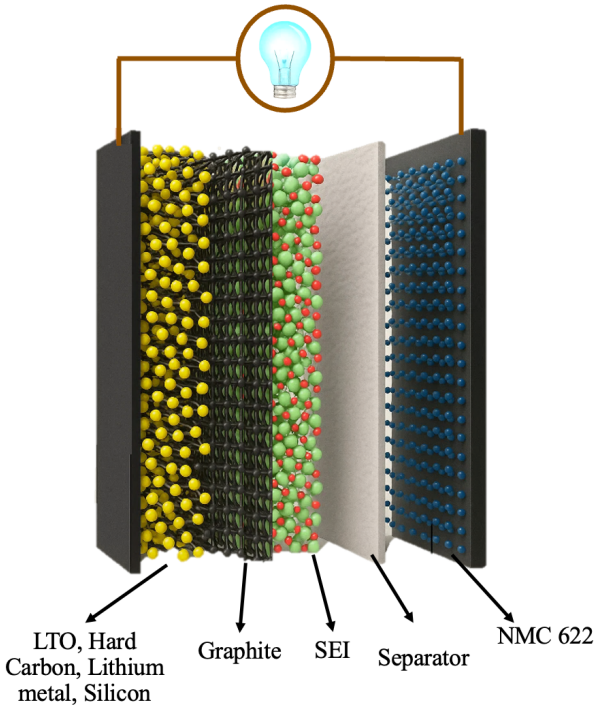

Figure 3.8. 3D schematic of a Li–ion battery with bilayer anode architecture and NMC622 cathode.

Subsequently, 16 simulations were carried out in which the second layer was varied using different materials, either in their pure form (100%) or as composites with graphite at 10%, 20%, and 30% concentrations. This approach aimed to evaluate four key response variables: capacity loss (%), SEI layer thickness (μm), potential drop over the SEI layer (mV), and electrolyte consumed (%).

The four configurations that exhibited the most favorable or boundary values were selected for further analysis and reported in Table 3.2. These boundary values were defined based on a reference point using pure graphite and data reported in the literature. For example, the maximum acceptable capacity loss was set at 20% after 2,000 cycles a value consistently reported as a typical upper limit in previous studies [60, 61].

All response variables were weighted equally when determining the optimal configurations. This selection enabled a direct comparison between the best–performing simulations and the graphite–based reference, providing a robust evaluation framework for material performance in multilayer anode architectures.

In Figure 3.9a presents four key metrics from these simulations, the dotted blue line representing the graphite anode shows how capacity retention declines steadily with cycling. Although initial capacity is high, each cycle irreversibly consumes a small fraction of lithium through SEI formation, reducing usable capacity. After 2 000 cycles, relative capacity falls to about 94 %, reflecting cumulative loss of active lithium. Introducing 20 % silicon in a bilayer design substantially boosts initial capacity without compromising retention. The bilayer graphite + Si anode retains around 83 % of its capacity after 2 000 cycles. This remarkable stability contrasts sharply with unprotected silicon anodes and arises because the outer graphite layer guides the main SEI formation and the silicon interlayer stores additional Li, alleviating deep lithiation stress on the graphite. In conventional mixed–blend graphite–Si electrodes, SEI can propagate uncontrollably over silicon surfaces, hastening failure problem avoided in this stratified architecture [62].

Table 3.2. Final simulation results by battery configuration using multiple materials.

Code	Alternative material (%)	Configuration	Loss capacity (%)	SEI layer thickness (µm)	Potential drop over SEI layer (mV)	Electrolyte consumed (%)
E1	**100%**	**30H–30G**	**5.9**	**0.2**	**17.5**	**20.8**
E2	100%	30LTO–30G	55.73	0.01	23.73	6.5
E3	100%	30ML–30G	89.6	1.05	8.88	54.7
E4	100%	30S–30G	82.95	0.0033	1.39	3.3
E5	10%	30H–30G	6.24	0.22	82.7	23
E6	20%	30H–30G	5.96	0.22	79.53	22.8
E7	30%	30H–30G	5.82	0.216	68	22.6
E8	**10%**	**30LTO–30G**	**11.01**	**0.17**	**79**	**19.2**
E9	20%	30LTO–30G	12.44	0.14	68.34	16.3
E10	30%	30LTO–30G	11.5	0.12	57	15
E11	10%	30ML–30G	11.25	0.53	28.347	27.9
E12	20%	30ML–30G	14.35	0.61	23.95	32.1
E13	**30%**	**30ML–30G**	**16.8**	**0.7**	**17.55**	**36.6**
E14	10%	30SG–30G	14.2	0.25	49.2	27.5
E15	**20%**	**30SG–30G**	**18.4**	**0.34**	**31.6**	**37.5**
E16	30%	30SG–30G	23.1	0.48	34.9	53.3

When hard carbon replaces the second layer, capacity retention improves still further, reaching about 95 % of the initial value. Hard carbon operates at higher potentials than graphite and establishes a porous SEI that quickly saturates, suppressing further solvent reduction and deep graphite lithiation. After the first–cycle loss, these composites exhibit modest fade over hundreds of cycles once micropores are passivated [63].

The graphite/lithium–metal hybrid displays a steeper decline, retaining near 85 % capacity after 2 000 cycles. In practice, hybrid cells suffer rapid fade once plated lithium becomes electrically isolated “dead Li,” with usable capacity falling below 80 % in fewer than 15 cycles in previous reports [64]. Repeated stripping leaves disconnected filaments that consume both active lithium and contact area. The

simulation reproduces this behavior, showing a modest first–cycle loss followed by a sustained slide as newly deposited Li detaches, though the 30 wt % Li metal content simulated compensates from dropping below 80 % with increased capacity.

Finally, adding 10 % LTO enhances structural stability but slightly reduces relative retention. Although LTO's "zero–strain" framework forms virtually no SEI, replacing 10 wt % high–capacity graphite (372 mAh/g) with lower–capacity LTO (175 mAh/g) dilutes reversible Li–host sites. Continuous SEI growth on the remaining graphite surface thus consumes a fixed lithium amount, which translates into a steeper relative fade when divided by a smaller initial capacity. Jung et al. confirm this geometric penalty and reveal an additional lithium–shuttle loss during open–circuit rests, as Li^+ migrates from low–voltage graphite (~0.1 V) into higher–voltage LTO (1.55 V) what explain ~5 % extra capacity loss after 1000 cycles compared with graphite alone [65].

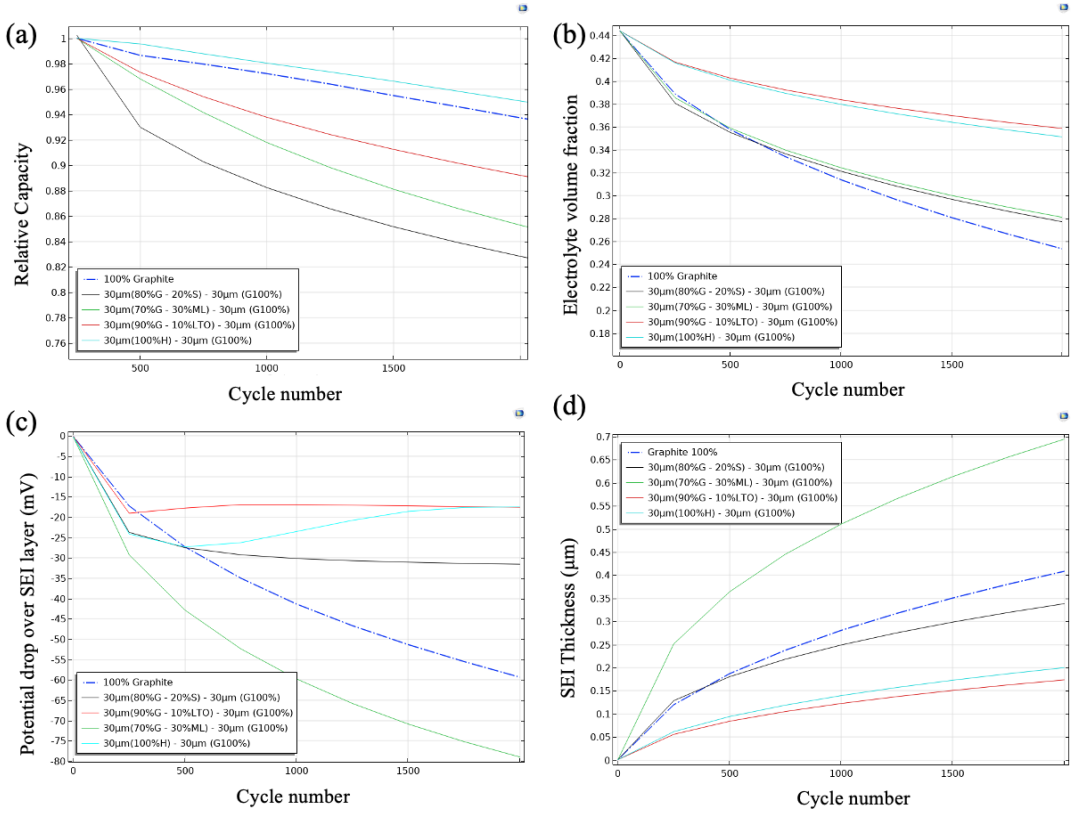

Figure 3.9. Comparative evolution of capacity (a), electrolyte volume fraction (b), potential drop over the SEI (c), and SEI thickness (d) in four different bilayer anode configurations.

The five curves in Figure 3.9b all start from the same electrolyte–volume fraction 0.44 at cycle 1 yet diverge markedly by cycle 2 000. Because only the outer 30 μm graphite layer of every bicomponent anode is in direct contact with the liquid electrolyte, differences in decay must arise from how the second layer modifies the way that graphite consumes solvent. In the reference cell the entire anode surface continuously reduces $LiPF_6$; carbonate fragments diffuse through an increasingly porous SEI and are converted to Li_2CO_3/LiF, so fraction declines almost linearly to 0.25, behavior that confirm the commercial graphite electrodes [66].

Substituting the inner half of the anode with hard carbon reduces the charge that the graphite must host at extreme low potentials; the outer layer therefore remains slightly less lithiated, generates fewer radicals and, once the highly porous hard–carbon matrix is passivated, solvent attack slows abruptly leaving at ≈ 0.35. With LTO slightly better preservation is achieved ≈ 0.36. LTO intercalates Li well above the carbonate reduction window, so that fraction of the anode never forms a classical SEI; in addition, its zero–strain lattice dampens stress in the overlying graphite, limiting crack–induced SEI renewal.

The graphite/Li–metal composite ends near 0.28 even though metallic Li is extremely reactive. The key is chronology: during formation, the sacrificial Li donates electrons that rapidly convert a portion of the solvent into a dense, LiF–rich SEI; once that compact layer is complete, solvent transport is kinetically hindered, and the slope flattens. Because only 30 μm of graphite remains exposed half the area of the 60 μm reference the ongoing consumption rate is lower than in the neat–graphite electrode, so the green trace ultimately sits above the blue one despite the violent early reaction. In other words, the bilayer strategy does work, since previous studies such as that developed by Zhang et al. (2025) report that the utilization of the lithium reserve falls to values below the typical 65 % with similar solvents such as EC:DMC [67].

The most surprising line is the graphite / 20 % Si, which still finishes above the 60 μm graphite baseline near 0.25. Two concurrent mechanisms explain this behavior. First,

halving the graphite thickness halves the area that can keep reducing solvent; the absolute amount of solvent consumed each cycle therefore drops even if the rate per unit area remains unchanged. Second, ≈ 15 % of the charge now enters the Si phase, so the graphite operates at a slightly higher average potential and generates fewer solvent–reduction radicals.

In Figure 3.9c (potential drop across the SEI) and Figure 3.9d (final SEI thickness) we observe how each bilayer anode modifies the response of the outer graphite even though the underlying kinetic expression is the same for all. The parasitic–current equation (Eq. 2.15) includes three parameters that here vary with the second layer: the expansion factor H_k, which amplifies the reaction rate when the graphite expands or cracks; the exchange current density J, which measures how fast the electrolyte is reduced at the surface; and the transfer coefficient α, which determines the sensitivity of that reduction to the overpotential.

With those adjustments each architecture generates an SEI of different thickness and resistivity. For example, for the 60 μm graphite layer (reference). Solid graphite exhibits moderate expansion and a constant J; its SEI grows quasi–linearly up to ~0.40 μm and ~ –60 mV after 2 000 cycles. For Graphite/Li–metal at the beginning, the sacrificial Li triggers a very high J and rapidly forms a dense LiF/Li_2O film with a thickness exceeds 0.7 μm and ~ –80 mV drops over SEI. For Graphite/hard carbon, the porous hard carbon absorbs part of the expansion, reducing H_k, and diverts a fraction of the current to slightly higher potentials. J and α remain in a middle range; the SEI stabilizes around 0.20 μm. The resulting resistance is low, hence the second–smallest polarization ~ –17 mV observed.

The LTO does not expand but the parasitic current is not eliminated, the graphite continues to operate very close to 0 V, so J is maintained and, with a relatively high α, with a thin film ~0.18 μm. However, its resistivity does not dominate over thickness and got a drop ~ –18 mV. Finally, in the configuration containing Graphite/20 % Si, the internal Si expands ~300 %, raising H_k and cyclically cracking the graphite SEI. Even so, the time that graphite spends in the most reducing regime is reduced, the film

reaches ~0.40 µm; and the polarization settles at ~ –32 mV, intermediate between hard carbon and solid graphite. Demonstrating once again that the strategy of using a graphite buffer improves the behavior of silicon.

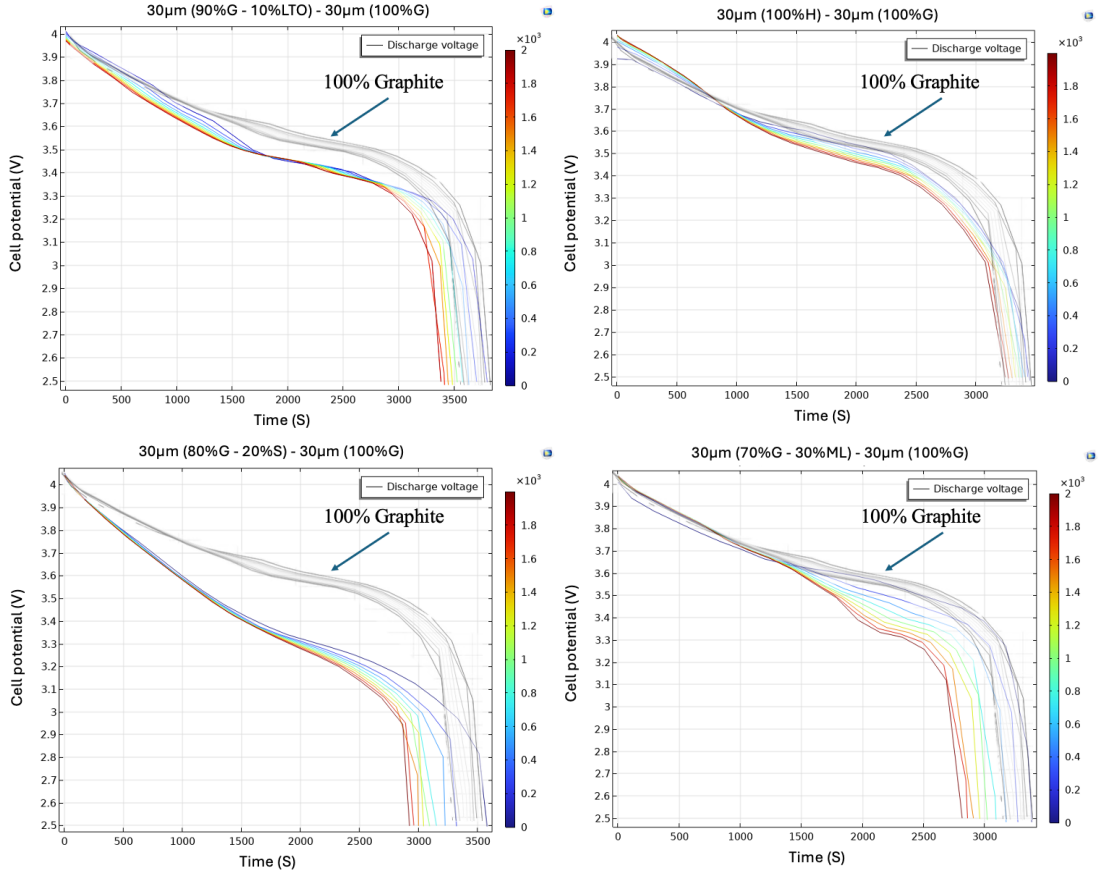

Figure 3.10. Cell potential evolution during discharge for (a) 30µm (90%G – 10%LTO) – 30µm (100%G), (b) 100% Graphite, (c) 30µm (80%G – 20%S) – 30µm (100%G), and (d) 30µm (70%G – 30%ML) – 30µm (100%G).

The multilayer anode (30 µm 90% G + 10% LTO / 30 µm graphite) exhibits a discharge profile ≈100–120 mV lower than the 60 µm graphite reference throughout the 1600–2600 s interval (Figure 3.10a). The offset originates from the intrinsic electrochemical potentials of the two active hosts. A layered NMC622 cathode remains near 4.2 V vs Li/Li^+ at full charge, while fully Lithiated graphite lies at ≈ 0.10 V vs Li/Li^+. LTO, in contrast, intercalates Li^+ at 1.55 V vs Li/Li^+ roughly 1.4 V higher than graphite. Incorporating only 10 wt % LTO into the outer layer therefore raises the mass–weighted average anode potential to ≈ 0.20–0.25 V. Because the cell voltage is simply $V = V_{cathode} - V_{anode}$, this ~0.10–0.15 V increase in anode potential subtracts

the same amount from the cell output, explaining the vertical gap observed in the mid–SOC plateau.

Independent three–electrode tests and physics–based simulations confirm that even ≤ 10 wt % LTO is sufficient to lift the anode potential and shorten the constant–current plateau by 80–150 mV at comparable rates [68]. Charge that pristine graphite would deliver below about 3.45 V (full–cell voltage) is now supplied by the LTO sub–phase at its higher equilibrium potential; the cell therefore enters the 3.40 V region sooner and maintains the 100–120 mV separation between the two voltage families throughout the 1500–3000 s window.

Beyond 2600 s a second trend emerges: the hybrid–anode curves fall more steeply than those of pure graphite. Once most graphite staging transitions are complete, the small LTO fraction becomes the kinetic bottleneck, its lower lithium diffusivity and larger activation overpotential increase electrode polarization so the voltage drops faster, and the cycle–to–cycle spread widens. In short, the hybrid design trades a modest slice of energy density during the 1600–2600 s segment for greater mechanical stability and present an additional polarization once the LTO phase governs the rate.

Figure 3.10b demonstrates that the multilayer anode with hard carbon provides a complementary Li storage mechanism to graphite. In the voltage window of 3.7–3.0 V (≈1000–3000s), the graphite/hard–carbon bilayer exhibits a discharge profile consistently ~50–80 mV lower than the 60 μm graphite benchmark. This offset is because hard carbon stores Li^+ over a broad sloping region that begins near 0.2–0.5 V vs Li/Li^+. Substituting 50 wt % of the active layer with hard carbon therefore raises the mass–weighted anode potential by ≈ 0.10 V; reproducing the slight observed in Figure 3.10b. Chen et al. shows similar results, a mixed graphite/hard–carbon anodes raise the average anode potential relative to pure graphite, which in turn lowers the mid–SOC cell voltage. Suggests the hybrid anode potential is ~60–80 mV higher than that of pure graphite at 0.5 C and this translates into an equivalent drop in cell voltage [69].

Both graphite and hard carbon are forms of carbon and thus have relatively small volume changes on cycling, graphite ~10% expansion, hard carbon often <5%. Unlike silicon or metallic lithium additions, hard carbon does not introduce acute expansion stress or massive SEI formation beyond the initial cycles. The primary degradation mechanism is gradual SEI growth on the large surface area of hard carbon pores, which can slowly increase internal resistance, and this is not the case, because it is protected by graphite. In fact, some studies have shown composite graphite/hard–carbon anodes to be highly stable over long cycling, with minimal capacity loss per cycle [70]. Consequently, their discharge voltage curves stay tightly clustered with cycling an expansion of the curves is minor. Indeed, the voltage profiles evolve only slightly with a small increase in polarization, because neither component suffers severe active material loss.

The hard carbon's sloping voltage contribution can even help maintain cell voltage in later cycles: as graphite capacity fades a bit, the hard carbon can still uptake/discharge lithium over a broad potential range, sustaining the cell's voltage output. Thus, divergence in the discharge curves tends to begin late in the discharge often near the end of discharge around ~3.0 V and remains minimal. The combination of robust graphite and resilient hard carbon yields an anode with excellent capacity retention and only slight impedance growth, explaining why its voltage profiles change very little even after extensive cycling.

In Figure 3.10c discharges ~150–200 mV below the 60 μm graphite reference from the very start of the run ≈ 0–2500 s. This downward offset is expected, because the Si domains begin alloying at ~0.40 V vs Li/Li^+ significantly higher than the 0.10 V plateau of graphite . The graphite "buffer" layer keeps the silicon physically isolated from the electrolyte during the first half of the discharge, so the cell retains the smooth, single–phase slope typical of graphite; in full–Si or Si/Gr blended electrodes that face the electrolyte directly, a voltage dip and large impedance rise usually appear within the first few cycles [71].

In the Si–rich multilayer the Li–induced volumetric expansion slows down solid–state diffusion and increases reaction over–potential. Multiphysics models of Si/graphite composites show that simply adding diffusion–induced stress to the reaction kinetics reproduces the sharp rise in polarization that occurs once silicon carries most of the current, without invoking particle cracking or extra SEI growth [72, 73]. The graphite buffer delays this kinetic bottleneck hence the stable segment up to 2500s but cannot prevent it once the Si capacity becomes dominant.

Since the Si plateau is at a higher anode potential, the cell offers greater capacity per unit cell voltage drop below 3.3 V in the 2000s (useful for applications that prioritize gravimetric energy over nominal voltage), but the faster polarization growth means it will reach its cut–off voltage sooner at high current rates. Whether that is advantageous depends on the duty cycle: for devices that exploit the extra Si capacity at modest C–rates such as portable electronics, the trade–off can be worthwhile, whereas for high–rate power tools the earlier voltage drop could be a problem.

The configuration of Figure 3.10d with metallic lithium traces the 60 μm–graphite baseline up to 3.5 V (0–1300 s), confirming that the graphite buffer effectively shields the metallic–Li domains during the early part of discharge. Once the graphite in the upper layer is largely delithiated, Li stripping begins in the layer containing 30% Li–rich domains. Because metallic Li has virtually zero Li–diffusion resistance but a higher interfacial over–potential than graphite, the anode potential rises more steeply; the full–cell voltage therefore bends downward by an extra 120–150 mV and the colored bundle widens between 3.5 V and 2.5 V.

Below 3.0V the curves remain separated but do not diverge catastrophically, even after 2000 simulated cycles. Two factors explain this numerical stability: Limited Li fraction (30 %) + graphite scaffold. Experiments on graphite/Li–metal hybrid anodes show that keeping the plated–Li inventory below ~35 % of the total capacity markedly improves reversibility and suppresses short–circuit events. Cells with a 25–30 % Li

overlay maintained 96 % of their initial capacity after 120 cycles at 1 C, whereas full Li–foil anodes failed within 30 cycles [74]. A similar capacity–buffer concept was demonstrated by Martin et al. cycling Li on graphite delivered a 20 % energy boost and >100 stable cycles without dendritic shorting Cell [64].

The layer with 30 % Li / 70 %G offers 30 % extra specific capacity with only a modest penalty in mid–SOC voltage. For applications that value gravimetric energy over constant–power output, for example, lightweight UAV packs the trade–off can be advantageous, whereas high–rate tools might suffer from the earlier voltage sag [75].

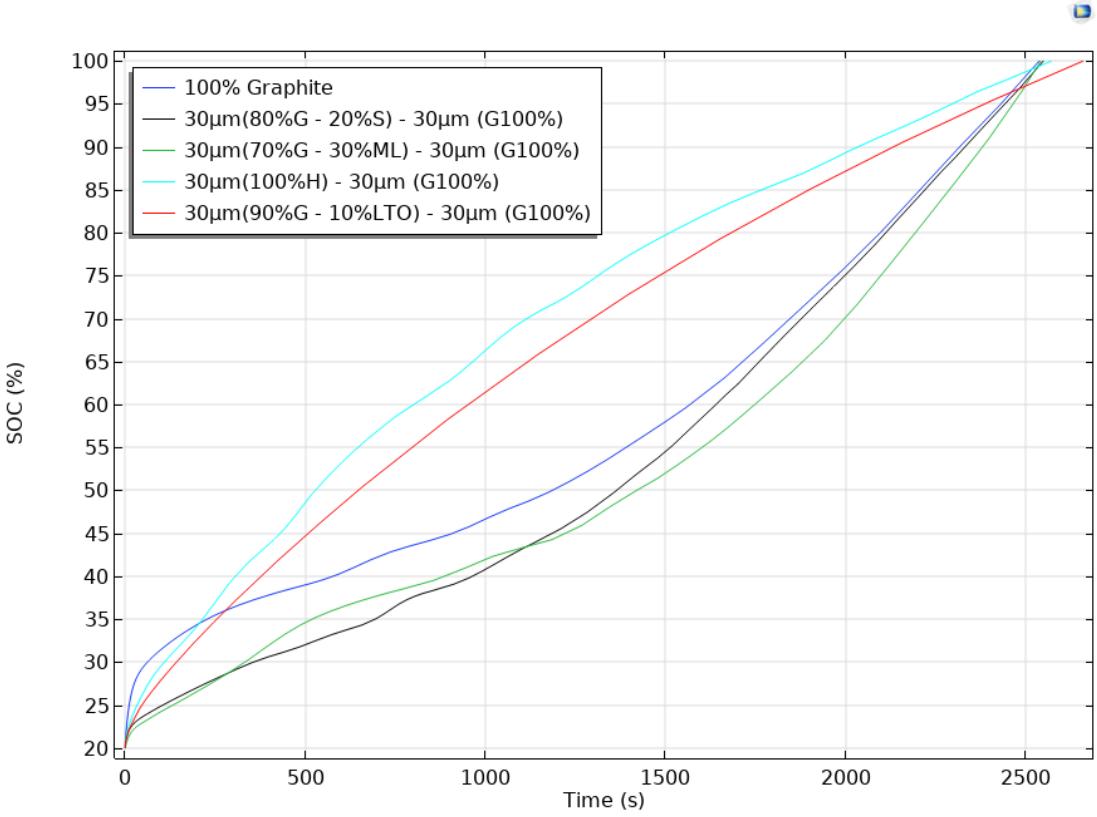

Figure 3.11. Voltage profiles during charging for different anode configurations with multiple materials, simulated in a 3D pouch cell.

Figure 3.11 compares the state–of–charge (SOC) evolution during the 2000th charge of five pouch cells that share an identical cathode/electrolyte set–up but differ in the architecture of a 60 µm anode. The blue trace represents the reference electrode, a monolithic 60 µm layer of graphite. Its curve shows the familiar profile of graphite

with a rapid rise during the initial stage's transitions, followed by a pronounced inflection after ≈500s as the material approaches full lithiation.

Introducing a bilayer design alters that behavior when the rear 30 μm are replaced by hard carbon (cyan curve), the cell reaches 50 % SOC in barely 500 s almost twice as fast as the reference. The disordered porosity of hard carbon accepts Li^+ at higher potentials (~0.1–0.2 V) and with lower diffusion resistance, so the outer graphite never sinks into the Li–plating regime; the graphite therefore retains a larger active surface area, and the overall impedance remains low throughout the charge. A similar but slightly less pronounced acceleration is observed for the red curve, where 10 % LTO is blended into the rear layer. LTO intercalates at 1.55 V and behaves as a kinetic buffer, taking up the initial current pulse, mitigating graphite polarization, and shortening the constant–voltage segment by roughly 15–20 %. This behavior is evident in the turquoise trace (90 % G + 10 % LTO).

By contrast, replacing the rear layer with 20 % Si (black) or 30 % Li metal (green) delays the rise in SOC. Silicon and plated lithium add substantial capacity, yet their interfacial kinetics are slower under 1C rate: Si suffers from sluggish solid–state diffusion, whereas Li plating must overcome a nucleation overpotential. Consequently, both curves lag until ≈1200 s, when the front graphite saturates and the current density across the rear layer drops to a level that these materials can sustain. Once that threshold is crossed, the black and green traces steepen and all cells finally converge near full charge at ≈2600 s, confirming that ultimate capacity is fixed by total active mass while the anode architecture dictates how quickly that capacity can be accessed.

Taken together, the plot demonstrates that a thin graphite front coupled to a fast–kinetics rear material (hard carbon or modest LTO doping) delivers the most balanced outcome: it preserves the high energy density of graphite while allowing a markedly steeper SOC ascent and mitigating Li–plating risk. Designs that instead prioritize extra capacity through Si or Li metal can match the final SOC but incur an early–stage

kinetic penalty that lengthens charge time under identical current constraints. These observations underline the practical advantage of multilayer anodes that decouple kinetic buffering from capacity storage, offering a clear pathway toward faster and safer charging protocols without sacrificing gravimetric energy.

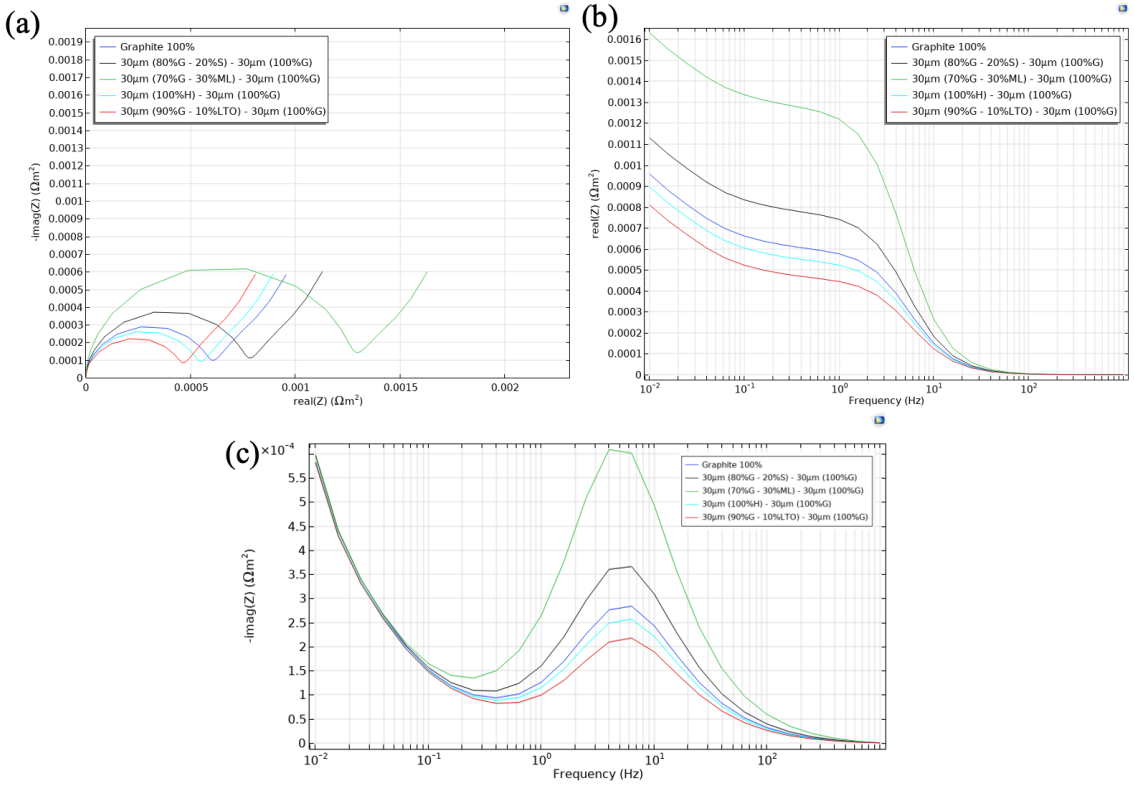

Figure 3.12. Electrochemical impedance response of multilayer anodes with various material combinations: (a) Nyquist plot, (b) Bode magnitude plot, and (c) Imaginary impedance vs. frequency.

Figure 3.12a presents the Nyquist response of the five simulated half–cells and immediately reveals how the inner layer governs the overall electrochemical footprint once the outer 30 µm graphite buffer is fixed. Diameter of each semicircle diverges in proportion to the transport penalties introduced by the second layer.

The monolithic 60 µm graphite reference defines the baseline; inserting 20% Si behind the buffer (black trace) widens the arc because lithiation of Si lowers electronic conductivity and produces elastic mismatch at the graphite/Si interface. However, it is a normal and natural process; an impedance study on cells with different contents of SiO_x/graphite demonstrated that with >10 wt% SiO_x, the progressive fracture of silicon particles and the continuous formation of SEI cause drastic increases in R_{ohm}, R_{SEI}, and

R_{ct}, correlated with rapid capacity degradation. Exceeding ~5–10% Si leads to accelerated loss of cyclability, suggesting a practical threshold for Si content in order not to compromise the conductivity of the percolation network [76]. It is important to highlight that in this simulation and under this strategy, values up to 20 wt% of pure silicon were achieved.

Substituting a 30% Li–metal domain (green) nearly doubles the diameter, a consequence of Li–ion starvation inside the plated layer that manifests as an additional Warburg component. Wang et al. (2021) observed similar trends in graphite/Li hybrid anodes: the accumulation of dendritic Li deposits rapidly increases impedance and consumes active lithium, accelerating capacity fade unless a robust artificial SEI is implemented through coating strategies and careful electrolyte selection [77]. By contrast, a 100% hard–carbon backing increases resistance only marginally; anodes with hard carbon as the inner layer tend to behave more similarly to graphite in terms of resistance, as they do not undergo abrupt phase transitions during Li^+ insertion, resulting in a more gradual change in charge–transfer resistance [78].

With 10% LTO, the composite narrows the arc, leveraging LTO's zero–strain lithiation and three–dimensional Li–ion pathways to preserve electronic percolation across the laminate. Lee et al. (2013) reported that spherical graphite coated with LTO showed better fast–charging capacity and longer cycle life at 25 °C and 55 °C compared to uncoated graphite, mainly because the LTO coating helped maintain low surface resistance during cycling [79]. Zhao et al. (2024) presented an EG/LTO composite with a capacity retention rate of 98.4%, even higher than that of hard carbons tested under the same conditions, which is attributed to the rapid Li^+ diffusion facilitated by the porosity of the EG/LTO structure, reducing interfacial resistance [80]. In summary, an electrochemically benign inner layer such as LTO minimizes the generation of additional resistance during fast charge/discharge, overcoming the kinetic limitations of conventional graphite.

In Figure 3.12b, the differences between configurations become more evident at low frequencies, where each trace reflects the total system resistance, consistent with the arcs observed in the Nyquist plot. The Li–metal laminate maintains the highest resistance across this band, indicating that ionic access to the plated domain is restricted to slow leakage through the outer graphite. The graphite–Si laminate exhibits a slightly higher impedance than the baseline, but it is moderate and because slower ionic diffusion in the lithiated Si phase and minor electronic network discontinuities that slow down internal charge transfer. Hard carbon is below the single–graphite baseline because its additional micro–porosity partially compensates for its poorer electronic conductivity, whereas the LTO–containing electrode persistently exhibits the lowest resistive, consistent with rapid transport within the structure.

Figure 3.12c shows the imaginary part of the impedance (–Im(Z)) as a function of frequency, providing insight into the dominant electrochemical time constants of each configuration. Unlike the Nyquist plot (Figure 3.12a), which focuses on the resistive and capacitive behavior in the complex plane, or the real part of the impedance in Figure 3.12b, this representation highlights the frequency at which the system stores the most energy before dissipating it. It is particularly useful for identifying how internal diffusion and interfacial kinetics affect the relaxation dynamics of each multilayer design.

All configurations display a main peak around 10 Hz, although with different magnitudes. The lithium–metal architecture (green line) reaches the highest peak, indicating greater charge accumulation and slower relaxation. The inclusion of 20% silicon (black line) also raises the peak height above the graphite reference, reflecting limited solid–state diffusivity and internal electronic bottlenecks. In contrast, the hard carbon laminate and the monolithic graphite (red and blue lines) cluster near the same frequency, with only a modest increase in peak height for hard carbon. The LTO–containing cell shows the lowest peak, consistent with its fast ionic transport and a stable internal structure that maintains an unperturbed interfacial response.

Taken together, the five impedance projections form a coherent hierarchy that becomes entirely rational once the intrinsic transport properties and volumetric stability of the hidden layer are considered. Because SEI growth is confined to the outer graphite, the multilayer strategy succeeds in decoupling interfacial side reactions from the high–capacity, high–stress phases beneath it. Performance is therefore dictated not by additional SEI resistance, but by the balance between electronic percolation and Li–ion diffusivity within the composite laminate. Materials that introduce minimal elastic strain and provide fast dual–conduction pathways such as LTO or hard carbon allow the buffer to surpass or match a monolithic graphite electrode, whereas phases that either swell dramatically (Si) or block ionic transport (Li metal) impose resistive penalties in exchange for extra capacity. This section therefore highlights a clear design rule for high–energy multilayer anodes: pair a graphite buffer with an inner layer that is both mechanically benign and intrinsically fast for Li transport if the goal is to outperform conventional graphite while preserving interfacial stability.

4. CHAPTER 4 – CONCLUSIONS AND PERSPECTIVES

This work demonstrates that a simulation–guided workflow combining finite–element electrochemical modelling in COMSOL Multiphysics® with multivariate statistics in JMP® can rationally engineer multilayer lithium–ion anodes that marry high specific capacity with long–term stability.

A full factorial study in Phase I established that the most balanced design consists of a 30 μm graphite buffer coated on the electrolyte side and a 30 μm graphite–silicon composite containing 20 wt % Si built with 2.5 μm graphite particles. After 2 000 cycles at 1 C, this bilayer limits capacity loss to 18.4 %, holds the SEI to 0.34 μm, restrains the SEI over–potential to 31.6 mV, and consumes only 37.5 % of the starting electrolyte.

Relative to a monolithic 60 μm graphite anode that fades 7.09 % while experiencing a 0.25 μm SEI and a larger 59 mV drop with 42.9 % solvent loss; the bilayer sacrifices some absolute retention but sharply curtails interfacial resistance and electrolyte depletion. It also outperforms a homogeneous 90 % G / 10 % Si slurry, which, despite only ≈16 % fade, accrues a 0.59 μm SEI, a 152 mV over–potential, and 62.7 % solvent loss because silicon is fully exposed to the electrolyte. The graphite skin therefore proves essential to moderate silicon–electrolyte interactions and distribute current uniformly.

Phase II retained this graphite front layer and replaced the hidden half–layer with alternative hosts. A 100 % hard–carbon core maintained 94.1 % of initial capacity (loss 5.9 %), built only a 0.20 μm SEI, limited the drop to 17.5 mV, and used 20.8 % electrolyte. Substituting a modest 10 wt % LTO delivered the thinnest SEI (0.17 μm) and the lowest solvent loss (19.2 %) at the cost of an 11.0 % capacity penalty, whereas embedding 30 wt % Li metal pushed gravimetric capacity highest but stabilized at 83.2 % retention with a 0.70 μm SEI and 36.6 % electrolyte consumption, signaling dead–

lithium formation under the graphite shield. Nyquist analyses confirm that once the graphite veneer fixes Rs and R_{SEI}, the diameter of the semicircle scales with the transport limitations of the hidden layer, decoupling SEI growth from charge–transfer resistance and leaving diffusional impedance to be dictated by the second material's mechanics and ion pathways.

Several constraints temper these findings. All simulations assumed isothermal operation at 25 °C, a fixed NMC622 cathode and a single EC/EMC electrolyte, omitting thermal gradients, cathode variability and electrolyte additives that could shift degradation pathways. Only primary intercalation and alloying reactions were implemented; secondary SEI chemistry, gas evolution and stress–induced cracking were excluded for computational tractability. Moreover, the study was confined to 60 μm total anode thicknesses and did not explicitly model mechanical deformation or binder fatigue, so scale–up to thicker electrodes or high–pressure calendaring may introduce additional failure modes.

Future work should therefore integrate thermo–mechanical coupling, extended reaction networks and in–plane heterogeneity to capture real pouch–cell conditions, corroborate the predicted optima through prototype fabrication and long–term cycling, and explore graded or tri–layer architectures that combine multiple high–capacity phases while preserving the graphite buffer. Investigating solid–state electrolytes, advanced binders and laser–patterned diffusion channels could further unlock silicon– and lithium–rich layers without compromising safety, while data–driven optimization of particle morphology and porosity offers a promising route to translate these computational insights into commercially viable high–energy batteries.

Nonetheless, the quantitative map obtained here offers a cost–efficient springboard for laboratory scale–up. The immediate next step is to fabricate coin–cell prototypes of the 30 μm G / 30 μm 20 % Si reference and the three best Phase II variants, validate the predicted SEI thickness, impedance and fade, then migrate the winning laminates to pouch cells where electrolyte volume, stack pressure and thermal management can be tuned. Iterative loops that couple high–throughput cycling data with model

inversion will shorten development cycles, while application–specific tailoring becomes straightforward: hard–carbon or LTO cores for fast–charge, long–life systems, and silicon– or Li–rich cores where gravimetric energy trumps constant–power output. In this sense, the project provides a decisive pre–selection that can reduce experimental costs and accelerate the transition from digital prototype to market–ready product.

Bibliography

[1] J.B. Goodenough, K.S. Park, The Li–ion rechargeable battery: a perspective, J. Am. Chem. Soc. 135 (2013) 1167–1176. https://doi.org/10.1021/ja3091438.

[2] Moores, S. (2021). The global battery arms race: Lithium–ion battery gigafactories and their supply chain. Oxford Institute for Energy Studies, https://www.oxfordenergy.org/wpcms/wpcontent/ uploads/2021/02/THE–GLOBAL–BATTERY–ARMS–RACE–LITHIUM–IONBATTERY– GIGAFACTORIES–AND–THEIR–SUPPLY–CHAIN.pdf.

[3] Wu, Y. (2015). Lithium–ion batteries: Fundamentals and applications. CRC Press. https://doi.org/10.1201/b18796.

[4] N. Nitta, F. Wu, J.T. Lee, G. Yushin, Li–ion battery materials: present and future, Mater. Today 18 (2015) 252–264. https://doi.org/10.1016/j.mattod.2014.10.040.

[5] J.M. Tarascon, M. Armand, Issues and challenges facing rechargeable lithium batteries, Nature 414 (2001) 359–367. https://doi.org/10.1038/35104644.

[6] M.N. Obrovac, V.L. Chevrier, Alloy negative electrodes for Li–ion batteries, Chem. Rev. 114 (2014) 11444–11502. https://doi.org/10.1021/cr500207g.

[7] S. Chae, M. Ko, K. Kim, K. Ahn, J. Cho, Confronting issues of the practical implementation of Si anode in high–energy lithium–ion batteries, Joule 1 (2017) 47–60. https://doi.org/10.1016/j.joule.2017.07.006.

[8] Wang, T., Wang, Z., Li, H., Cheng, L., Wu, Y., Liu, X., Meng, L., Zhang, Y., & Jiang, S. (2024). Recent status, key strategies, and challenging prospects for fast charging silicon–based anodes for lithium–ion batteries. Carbon, 230, 119615. https://doi.org/10.1016/j.carbon.2024.119615.

[9] He, W., Xu, W., Li, Z., Hu, Z., Yang, J., Qin, G., Teng, W., Zhang, T., Zhang, W., Sun, Z., & Yu, X. (2025). Structural design and challenges of micron–scale silicon–based lithium–ion batteries. Advanced Science, 12(6), e2407540. https://doi.org/10.1002/advs.202407540.

[10] Y. Liu, K. Hanai, J. Yang, N. Imanishi, A. Hirano, Y. Takeda, Silicon/carbon composites as anode materials for Li–ion batteries, Electrochem. Solid–State Lett. 7 (2004) A369–A372. https://doi.org/10.1149/1.1795031.

[11] H. Kim, M. Seo, M.–H. Park, J. Cho, A critical size of silicon nano–anodes for lithium rechargeable batteries, Angew. Chem. Int. Ed. 49 (2010) 2146–2149. https://doi.org/10.1002/anie.200906287.

[12] K. Evanoff, A. Magasinski, J. Yang, G. Yushin, Nanosilicon–coated graphene granules as anodes for Li–ion batteries, Adv. Energy Mater. 1 (2011) 495–498. https://doi.org/10.1002/aenm.201100071.

[13] E. Barcaro, V. Marangon, M. Mutarelli, J. Hassoun, A lithium–ion battery with cycling stability promoted by the progressive activation of a silicon oxide anode in graphene–amorphous carbon matrix, J. Power Sources 595 (2024) 234059. https://doi.org/10.1016/j.jpowsour.2024.234059.

[14] Z. Karkar, M.S.E. Houache, C.–H. Yim, Y. Abu–Lebdeh, An industrial perspective and intellectual property landscape on solid–state battery technology with a focus on solid–state electrolyte chemistries, Batteries 10 (2024) 24. https://doi.org/10.3390/batteries10010024.

[15] J. Tang, Progress in the application of silicon–based anode nanotechnology in lithium batteries, E3S Web Conf. 553 (2024) 01007. https://doi.org/10.1051/e3sconf/202455301007.

[16] Chan, C. K., Peng, H., Liu, G., McIlwrath, K., Zhang, X. F., Huggins, R. A., & Cui, Y. (2008). High–performance lithium battery anodes using silicon nanowires. Nature Nanotechnology, 3(1), 31– 35. https://doi.org/10.1038/nnano.2007.411.

[17] Liu, D.–H., Bai, Z., Li, M., Yu, A., Luo, D., Liu, W., Yang, L., Lu, J., Amine, K., & Chen, Z. (2020). Developing high safety Li–metal anodes for future high–energy Li–metal batteries: Strategies and perspectives. Chemical Society Reviews, 49(15), 5407–5445. https://doi.org/10.1039/C9CS00636B.

[18] Nezamzadeh Ezhyeh, Z., Khodaei, M., & Torabi, F. (2023). Review on doping strategy in $Li_4Ti_5O_{12}$ as an anode material for lithium–ion batteries. Ceramics International, 49(5), 7105–7141. https://doi.org/10.1016/j.ceramint.2022.04.340.

[19] Xie, L., Tang, C., Bi, Z., Song, M., Fan, Y., Yan, C., Li, X., Su, F., Zhang, Q., & Chen, C. (2021). Hard carbon anodes for next–generation Li–ion batteries: Review and perspective. Advanced Energy Materials, 11(33), https://doi.org/10.1002/aenm.202101650.

[20] S. Yuan, Q. Lai, X. Duan, and Q. Wang, "Carbon–based materials as anode materials for lithium–ion batteries and lithium–ion capacitors: A review," J. Energy Storage, vol. 61, p. 106716, Jan. 2023, doi: 10.1016/j.est.2023.106716.

[21] Choi, J.–H., Ryu, W.–H., Park, K., Jo, J.–D., Jo, S.–M., Lim, D.–S., & Kim, I.–D. (2014). Multi–layer electrode with nano–$Li_4Ti_5O_{12}$ aggregates sandwiched between carbon nanotube and graphene networks for high–power Li–ion batteries. Scientific Reports, 4, 7334. https://doi.org/10.1038/srep07334.

[22] Ming, J., Li, M., Kumar, P., & Li, L.–J. (2016). A multilayer approach for advanced hybrid lithium battery. ACS Nano, 10(6), 6037–6044. https://doi.org/10.1021/acsnano.6b01626.

[23] M. Su, H. Wan, Y. Liu, W. Xiao, A. Dou, Z. Wang, H. Guo, Multi–layered carbon coated Si–based composite as anode for lithium–ion batteries, Powder Technol. 323 (2018) 294–300. https://doi.org/10.1016/j.powtec.2017.09.005.

[24] Hamedi, A.–S., Yao, A., Martin, R., Roig, R., Rivas Valadez, M., Pile, D., Shellikeri, A., Liu, B., & Wheeler, D. R. (2023). Multi–layer anodes for high–current applications. Electrochimica Acta, 439, 141649. https://doi.org/10.1016/j.electacta.2022.141649.

[25] Ko, K.–Y., Sung, K.–W., & Ahn, H.–J. (2024). Layer–by–layer–structured silicon–based electrode design for ultrafast lithium–ion batteries. Korean Journal of Chemical Engineering. Advance online publication. https://doi.org/10.1007/s11814–024–00357–1.

[26] Yuan, Y., Hu, R., Wang, W., Wang, Y., Zhang, T., & Wang, Z. (2025). Design and fabrication of high–performance multilayer silicon–carbon composite anodes for lithiumion batteries via femtosecond laser. Journal of Energy Storage, 110, 115362. https://doi.org/10.1016/j.est.2025.115362.

[27] Lin, D., Liu, Y., Liang, Z., Lee, H.–W., Sun, J., Wang, H., Yan, K., Xie, J., & Cui, Y. (2016). Layered reduced graphene oxide with nanoscale interlayer gaps as a stable host for lithium metal anodes. Nature Nanotechnology, 11, 626–632. https://doi.org/10.1038/nnano.2016.32.

[28] Bai, M., Xie, K., Yuan, K., Zhang, K., Li, N., Shen, C., Lai, Y., Vajtai, R., Ajayan, P., & Wei, B. (2018). A scalable approach to dendrite–free lithium anodes via spontaneous reduction of spray–coated graphene oxide layers. Advanced Materials, 30(29), 1801213. https://doi.org/10.1002/adma.201801213.

[29] Y. Guo, Y. Wei, H. Li, T. Zhai, Layer structured materials for advanced energy storage and conversion, Small 13 (2017) 1701649. https://doi.org/10.1002/smll.201701649.

[30] Sharma, N., Puthusseri, D., Ottakam Thotiyl, M., & Ogale, S. (2017). Hard carbon and $Li_4Ti_5O_{12}$–based physically mixed anodes for superior Li–battery performance with significantly reduced Li content: A case of synergistic materials cooperation. ACS Omega, 2, 8818–8824. https://doi.org/10.1021/acsomega.7b01659.

[31] Wang, Z., VahidMohammadi, A., Ouyang, L., Erlandsson, J., Tai, C.–W., Wågberg, L., & Hamedi, M. M. (2020). Layer–by–layer self–assembled nanostructured electrodes for lithium–ion batteries. Small, 17(4), 2006434. https://doi.org/10.1002/smll.202006434.

[32] Rist, U., Falkowski, V., & Pfleging, W. (2023). Electrochemical properties of laser–printed multilayer anodes for lithium–ion batteries. Nanomaterials, 13(17), 2411. https://doi.org/10.3390/nano13172411.

[33] Bläubaum, L., Röder, F., Nowak, C., Chan, H. S., Kwade, A., & Krewer, U. (2020). Impact of particle size distribution on performance of lithium-ion batteries. ChemElectroChem, 7(23), 4755–4766. https://doi.org/10.1002/celc.202001249.

[34] Gottschalk, L., Müller, J., Schoo, A., Baasch, E., & Kwade, A. (2024). Spherical graphite anodes: Influence of particle size distribution and multilayer structuring in lithium–ion battery cells. Batteries, 10(2), 40. https://doi.org/10.3390/batteries10020040.

[35] Luo, M., Mijailovic, A. S., Wang, G., Wu, Q., Sheldon, B. W., & Lu, W. (2024). Understanding particle size effect on fast–charging behavior of graphite anode using ultra–thin–layer electrodes. Journal of Energy Storage, 104, 114521. https://doi.org/10.1016/j.est.2024.114521.

[36] Geng, S., Zhou, J., Tan, B., Zheng, B., & Zhang, K. (2024). Impact of thickness and charge rate on the electrochemical performance of Si–based electrodes. Cell Reports Physical Science, 5(12), 102305. https://doi.org/10.1016/j.xcrp.2024.102305.

[37] Nasajpour–Esfahani, N., Garmestani, H., Bagheritabar, M., Jasim, D. J., Toghraie, D., Dadkhah, S., & Firoozeh, H. (2024). Comprehensive review of lithium–ion battery materials and development challenges. Renewable and Sustainable Energy Reviews, 203, 114783. https://doi.org/10.1016/j.rser.2024.114783.

[38] Xiao, P., Yun, X., Chen, Y., Guo, X., Gao, P., Zhou, G., & Zheng, C. (2023). Insights into the solvation chemistry in liquid electrolytes for lithium–based rechargeable batteries. Chemical Society Reviews, 52(15), 5255–5316. https://doi.org/10.1039/D3CS00151B.

[39] Nitta, N., & Yushin, G. (2014). High–capacity anode materials for lithium–ion batteries: Choice of elements and structures for active particles. Particle & Particle Systems Characterization, 31(3), 317–336. https://doi.org/10.1002/ppsc.201300231.

[40] Lazanas, A. C., & Prodromidis, M. I. (2023). Electrochemical impedance spectroscopy : A tutorial. ACS Measurement Science Au, 3(2), 162–193. https://doi.org/10.1021/acsmeasuresciau.2c00070.

[41] COMSOL. (2020). Battery design module user's guide (Version 5.6). COMSOL. https://doc.comsol.com/5.6/doc/com.comsol.help.battery/BatteryDesignModuleUsersGuide.pdf.

[42] D. Li, D. Danilov, Z. Zhang, H. Chen, Y. Yang, P.H.L. Notten, Modeling the SEI–formation on graphite electrodes in LiFePO4 batteries, J. Electrochem. Soc. 162 (2015) A858–A869. https://doi.org/10.1149/2.0161506jes.

[43] L. Cai, R.E. White, Mathematical modeling of a lithium–ion battery, in: Proceedings of the COMSOL Conference 2009, Boston, MA, 2009, Retrieved from https://www.comsol.com/paper/mathematical–modeling–of–a–lithium–ion–battery–6678 (accessed 13 December 2024).

[44] Wang, A., Kadam, S., Li, H., Shi, S., & Qi, Y. (2018). Review on modeling of the anode solid electrolyte interphase (SEI) for lithium–ion batteries. npj Computational Materials, 4, 15. https://doi.org/10.1038/s41524–018–0064–0.

[45] Alrashdan, M. H. S. (2024). Exchange current density at the positive electrode of lithium–ion batteries optimization using the Taguchi method. Journal of Solid State Electrochemistry, 28(1), 213–227. https://doi.org/10.1007/s10008–023–05672–x.

[46] COMSOL. (2020). Capacity fade due to SEI layer formation (Version 5.6). COMSOL. https://doc.comsol.com/5.6/doc/com.comsol.help.models.battery.capacity_fade/models.battery.capacity_fade.pdf.

[47] Ambrock, K., Ruttert, M., Vinograd, A., Billmann, B., Yang, X., Placke, T., Winter, M., & Börner, M. (2022). Optimization of graphite/silicon–based composite electrodes for lithium–ion batteries regarding the interdependencies of active and inactive materials. Journal of Power Sources, 552, 232252. https://doi.org/10.1016/j.jpowsour.2022.232252.

[48] M. Raić, K. Kvastek, L. Mikac, N. Baran, M. Ivanda, The effects of silicon anode thickness on the electrochemical performance of Li–ion batteries, Batteries 9 (2023) 173. https://doi.org/10.3390/batteries9030173.

[49] Horstkötter, I., & Bäker, B. (2023). An application–oriented lithium–ion battery degradation modelling framework for ageing prediction. Journal of Energy Storage, 60, 106640. https://doi.org/10.1016/j.est.2023.106640.

[50] Andersen, H. F., Foss, C. E. L., Voje, J., & Svensson, A. M. (2019). Silicon–carbon composite anodes from industrial battery grade silicon. Scientific Reports, 9, 14814. https://doi.org/10.1038/s41598–019–51324–4.

[51] Jha, V., & Krishnamurthy, B. (2022). Modeling the SEI layer formation and its growth in lithium–ion batteries (LiB) during charge–discharge cycling. Ionics, 28(8), 3661–3670. https://doi.org/10.1007/s11581–022–04617–0.

[52] Bashirpour–bonab, H. (2023). Investigation and electrochemical analysis of SEI layer formation in natural graphite anode formation process in lithium–ion battery. e–Prime – Advances in Electrical Engineering, Electronics and Energy, 5, 100261. https://doi.org/10.1016/j.prime.2023.100261.

[53] Wan, Y., Zhang, X., Li, M., Chen, J., & Wang, L. (2023). Modeling the impact of electrode material structure on the performance of lithium–ion batteries: Effects of porosity and particle size, In Proceedings of the 2023 7th International Conference on Smart Grid and Smart Cities (ICSGSC) (pp. 326–331). IEEE. https://doi.org/10.1109/ICSGSC59580.2023.10319130.

[54] Alvira, D., Antorán, D., Darjazi, H., Elia, G. A., Gerbaldi, C., Sebastian, V., & Manyà, J. J. (2025). High performing and sustainable hard carbons for Na–ion batteries through acid–catalysed hydrothermal carbonisation of vine shoots, Journal of Materials Chemistry A, 13(5), 2730–2741. https://doi.org/10.1039/D4TA07393B.

[55] Lochab, S., Bharathraj, S., Mayya, K. S., Barpanda, P., & Adiga, S. P. (2024). Unveiling the degradation mechanism of sodium ion batteries based on $Na_4Fe_3(PO_4)_2P_2O_7$ cathode and hard carbon anode suggests anode particle size, reduction for cycling stability. Batteries & Supercaps, 7(8), e202400025. https://doi.org/10.1002/batt.202400025.

[56] Julien, C. M., & Mauger, A. (2024). Fabrication of $Li_4Ti_5O_{12}$ (LTO) as anode material for Li–ion batteries. Micromachines, 15(3), 310. https://doi.org/10.3390/mi15030310.

[57] Acebedo, B., Cid, R., de Lasen–Tejada, M., Morant–Miñana, M. C., Fallarino, L., Goikolea, E., Rikarte, J., Gonzalo, E., & Ruiz de Larramendi, I. (2024). On the role of ultrathin lithium metal anodes produced by thermal evaporation, Journal of Power Sources, 618, 235218. https://doi.org/10.1016/j.jpowsour.2024.235218.

[58] Refino, A.D., Adhitama, E., Bela, M.M. et al. Impact of exposing lithium metal to monocrystalline vertical silicon nanowires for lithium–ion microbatteries. Commun Mater 4, 58 (2023). https://doi.org/10.1038/s43246–023–00385–0.

[59] Patil, R., Phadatare, M., Blomquist, N., Örtegren, J., Hummelgård, M., Meshram, J., Dubal, D., & Olin, H. (2021). Highly stable cycling of silicon–nanographite aerogel–based anode for lithium–ion batteries. ACS Omega, 6(10), 6600–6606. https://doi.org/10.1021/acsomega.0c05214.

[60] Saxena, S., Hendricks, C., & Pecht, M. (2016). Cycle life testing and modeling of graphite/$LiCoO_2$ cells under different state of charge ranges. Journal of Power Sources, 327, 394–400. https://doi.org/10.1016/j.jpowsour.2016.07.057.

[61] Rikka, V. R., Sahu, S. R., Chatterjee, A., Prakash, R., Sundararajan, G., & Gopalan, R. (2022). Enhancing cycle life and usable energy density of fast charging $LiFePO_4$–graphite cell by regulating electrodes' lithium level. iScience, 25(9), 104831. https://doi.org/10.1016/j.isci.2022.104831.

[62] Toki, G. F. I., Hossain, M. K., Rehman, W. U., Manj, R. Z. A., Wang, L., & Yang, J. (2024). Recent progress and challenges in silicon–based anode materials for lithium–ion batteries. Industrial Chemistry & Materials, 2, 226–269. https://doi.org/10.1039/D3IM00115F.

[63] Liao X, Hu D, Yu L, Li B, Xiao F, Wang S (2024) Spherical hard carbon/graphite anode for high performance lithium ion batteries. PLoS ONE 19(12): e0311943. https://doi.org/10.1371/journal.pone.0311943.

[64] Martin, C., Genovese, M., Louli, A. J., Weber, R., & Dahn, J. R. (2020). Cycling lithium metal on graphite to form hybrid lithium–ion/lithium metal cells. Joule, 4(6), 1296–1310. https://doi.org/10.1016/j.joule.2020.04.016.

[65] Jung, H.–G., Kim, J., Scrosati, B., & Sun, Y.–K. (2011). Micron–sized, carbon–coated $Li_4Ti_5O_{12}$ as high power anode material for advanced lithium batteries. Journal of Power Sources, 196(18), 7763–7766. https://doi.org/10.1016/j.jpowsour.2011.04.019.

[66] Asenbauer, J., Eisenmann, T., Kuenzel, M., Kazzazi, A., Chen, Z., & Bresser, D. (2020). The success story of graphite as a lithium–ion anode material – Fundamentals, remaining challenges, and recent developments including silicon (oxide) composites, Sustainable Energy & Fuels, 4(11), 5387–5416. https://doi.org/10.1039/D0SE00175A.

[67] Zhang, Y., Shen, H., Li, Y., Hu, Y., & Li, Y. (2025). Prelithiation strategies for enhancing the performance of lithium–ion batteries. RSC Advances, 15, 1249–1274. https://doi.org/10.1039/D4RA08234F.

[68] Fu, R., Zhou, X., Fan, H., Blaisdell, D., Jagadale, A., Zhang, X., & Xiong, R. (2017). Comparison of lithium–ion anode materials using an experimentally verified physics–based electrochemical model. Energies, 10(12), 2174. https://doi.org/10.3390/en10122174 .

[69] Chen, K.–H., Goel, V., Namkoong, M. J., Wied, M., Müller, S., Wood, V., Sakamoto, J., Thornton, K., & Dasgupta, N. P. (2021). Enabling 6C fast charging of Li–ion batteries with graphite/hard carbon hybrid anodes. Advanced Energy Materials, 1(5), 2003336. https://doi.org/10.1002/aenm.202003336.

[70] Yin, Y. , Shen, C. , Yturriaga, S. and Zheng, J. (2021) The Power–Energy Coupling Effect of Mixed Hard–Carbon/Graphite Anode. Journal of Materials Science and Chemical Engineering, 9, 16–31. doi: 10.4236/msce.2021.91002.

[71] Durdel, A., Friedrich, S., Hüsken, L., & Jossen, A. (2023). Modeling silicon–dominant anodes: Parametrization, discussion, and validation of a Newman–type model. Batteries, 9(11), 558. https://doi.org/10.3390/batteries9110558.

[72] Dhillon, S., Hernández, G., Wagner, N. P., Svensson, A. M., & Brandell, D. (2021). Modelling capacity fade in silicon–graphite composite electrodes for lithium–ion batteries. Electrochimica Acta, 377, 138067. https://doi.org/10.1016/j.electacta.2021.138067.

[73] Chen, Y., Yang, L., Guo, F., Liu, D., Wang, H., Lu, J., Zheng, J., Yu, X., & Li, H. (2022). Mechanical–electrochemical modeling of silicon–graphite composite anode for lithium–ion batteries. Journal of Power Sources, 527, 231178. https://doi.org/10.1016/j.jpowsour.2022.231178.

[74] Wu, Z., Wang, Z., Zhang, J., Bai, Z., Zhao, L., Li, R., Yang, Z., Bai, Y., & Sun, K. (2023). Decline mechanism of graphite/lithium metal hybrid anode and its stabilization by inorganic–rich solid electrolyte interface. ACS Applied Materials & Interfaces, 15(29), 34922–34930. https://doi.org/10.1021/acsami.3c05630.

[75] Xiao, C., Wang, B., Zhao, D., & Wang, C. (2023). Comprehensive investigation on lithium batteries for electric and hybrid–electric unmanned aerial vehicle applications. Thermal Science and Engineering Progress, 38, 101677. https://doi.org/10.1016/j.tsep.2023.101677 .

[76] Wang, X., Zhu, J., Dai, H., Yu, C., & Wei, X. (2023). Impedance investigation of silicon/graphite anode during cycling. Batteries, 9(5), 242. https://doi.org/10.3390/batteries9050242.

[77] Wang, S., Liu, D., Cai, X., Zhang, L., Liu, Y., Qin, X., Zhao, R., Zeng, X., Han, C., Zhan, C., Kang, F., & Li, B. (2021). Promoting the reversibility of lithium ion/lithium metal hybrid graphite anode by regulating solid electrolyte interface, Nano Energy, 90, 106510. https://doi.org/10.1016/j.nanoen.2021.106510.

[78] Goel, V., Masel, K., Chen, K.–H., Safdari, A., Dasgupta, N. P., & Thornton, K. (2025). The origin of the superior fast–charging performance of hybrid graphite/hard carbon anodes for Li–ion batteries. Energy Storage Materials, 76, 104053. https://doi.org/10.1016/j.ensm.2025.104053.

[79] Lee, M.–L., Li, Y. H., Liao, S.–C., Chen, J.–M., Yeh, J.–W., & Shih, H. C. (2013). $Li_4Ti_5O_{12}$–coated graphite anode materials for lithium–ion batteries. Electrochimica Acta, 112, 529–534. https://doi.org/10.1016/j.electacta.2013.08.150.

[80] Zhao, J., Zhu, X., Zhang, W., Qiu, J., Zhai, F., Zhang, H., Cao, G., Gao, S., Ding, F., & Xiang, Y. (2024). Expanded graphite incorporated with $Li_4Ti_5O_{12}$ nanoparticles as a high–rate lithium–ion battery anode. RSC Advances, 14, 14, 11276–11283. https://doi.org/10.1039/D4RA00832D.